

UCSF

UC San Francisco Previously Published Works

Title

A single-cell atlas of the normal and malformed human brain vasculature

Permalink

<https://escholarship.org/uc/item/2gg255fb>

Journal

Science, 375(6584)

ISSN

0036-8075

Authors

Winkler, Ethan A
Kim, Chang N
Ross, Jayden M
[et al.](#)

Publication Date

2022-03-04

DOI

10.1126/science.abi7377

Peer reviewed

RESEARCH ARTICLE SUMMARY

NEUROGENOMICS

A single-cell atlas of the normal and malformed human brain vasculature

Ethan A. Winkler[†], Chang N. Kim[†], Jayden M. Ross, Joseph H. Garcia, Eugene Gil, Irene Oh, Lindsay Q. Chen, David Wu, Joshua S. Catapano, Kunal Raygor, Kazim Narsinh, Helen Kim, Shantel Weinsheimer, Daniel L. Cooke, Brian P. Walcott, Michael T. Lawton, Nalin Gupta, Berislav V. Zlokovic, Edward F. Chang, Adib A. Abila*, Daniel A. Lim*, Tomasz J. Nowakowski*

INTRODUCTION: The cerebrovasculature delivers nourishment and regulates blood-brain molecular exchanges that are necessary for neurologic function. Coordinated communications between multiple cell types—including endothelium, pericytes, smooth muscle cells, and perivascular fibroblasts—provides the basis for the functional specialization of arteries, capillaries, and veins. Cellular dysfunction results in cerebrovascular diseases, a leading cause of death and disability. However, we currently lack a comprehensive atlas of cerebrovascular cells in the human brain. Further understanding of disease mechanisms and therapeutic strategies requires a deeper knowledge of cerebrovascular cells in humans.

RATIONALE: To provide a human cerebrovascular cell atlas, we used single-cell mRNA sequencing (scRNA-seq), using dissociated vascular cells isolated from the adult human brain and arteriovenous malformations (AVMs), a cerebrovascular disease of arteriovenous patterning in which patients are prone to bleeding and stroke. Using marker genes identified from single-cell transcriptomes, we characterized

spatial distributions of cerebrovascular cell states with multiplexed fluorescent in situ hybridization and immunostaining. Joint comparative analyses between scRNA-seq datasets systematically profiled patterns of aberrant gene expression in AVMs. To investigate potential relevance of these findings, we performed in silico analyses to catalog dysregulated cell-to-cell interactions and to resolve cell states enriched in advanced stages of AVMs that bled. Predictions were validated with immunostaining and functional assays in cell culture.

RESULTS: By performing scRNA-seq on 181,388 individual cells, we identified more than 40 transcriptomically defined cell states of vascular, immune, and neighboring glial or neuronal cells from the human adult cerebrovasculature and AVMs. Iterative analyses of single-cell gene expression profiles revealed endothelial molecular signatures underlying arteriovenous phenotypic changes called zonation. Our study uncovered an expanded diversity of perivascular cells in human but not mouse brain, transcriptional variation within smooth muscle

cells and perivascular fibroblasts, and the presence of smooth muscle-like cells known as fibromyocytes. In AVMs, our data suggested a loss of normal zonation among endothelial cells. Moreover, we observed the emergence of a distinct transcriptomic state that corresponded to the nidus, which was characterized by heightened angiogenic potential and immune cell cross-talk. In addition, we characterized the cellular ontology of the cerebrovasculature-derived immune cell response and identified infiltration of distinct immune cell states, such as *GPNMB*⁺ monocytes, which contribute to depletion of stabilizing smooth muscle cells in AVMs that bled.

CONCLUSION: Our single-cell atlas highlights the transcriptomic heterogeneity underlying cell function and interaction in the human cerebrovasculature and defines molecular and cellular perturbations in AVMs, a leading cause of stroke in young people. The identified interplay between vascular and immune cells may aid the development of therapeutic programs in vascular malformations. More broadly, this cell atlas should inform future studies in other human diseases to accelerate mechanistic understanding and therapeutic targeting of the human cerebrovasculature and its diseases. ■

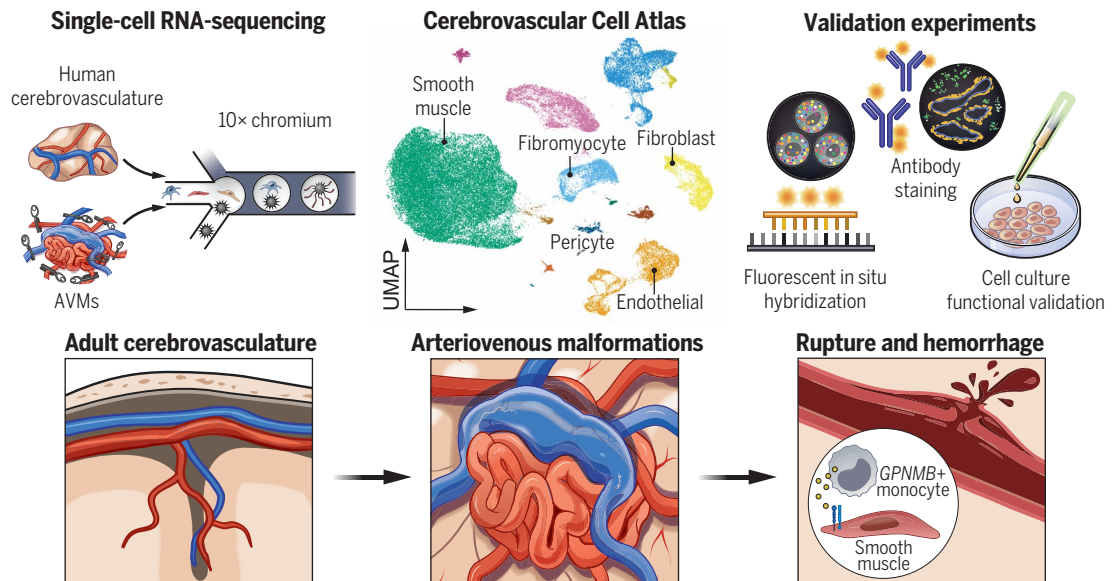
The list of author affiliations is available in the full article online.
*Corresponding author. Email: adib.abila@ucsf.edu (A.A.A.); daniel.lim@ucsf.edu (D.A.L.); tomasz.j.nowakowski@gmail.com (T.J.N.)

[†]These authors contributed equally to this work.

Cite this article as E. A. Winkler et al., *Science* 375, eabi7377 (2022). DOI: 10.1126/science.abi7377

S READ THE FULL ARTICLE AT <https://doi.org/10.1126/science.abi7377>

The adult human cerebrovascular cell atlas. We used scRNA-seq to assemble a cerebrovascular cell atlas from the adult human brain and AVMs. Findings were then experimentally validated. Comparative analyses revealed endothelial molecular transformations and heightened immune cell response in AVMs. Using this cell atlas, we identified immune cell states implicated in AVM rupture and brain hemorrhage.



RESEARCH ARTICLE

NEUROGENOMICS

A single-cell atlas of the normal and malformed human brain vasculature

Ethan A. Winkler^{1,2,3,4,†}, Chang N. Kim^{2,3,5,6,†}, Jayden M. Ross^{1,2,3,5,6}, Joseph H. Garcia¹, Eugene Gil^{1,2}, Irene Oh⁷, Lindsay Q. Chen⁷, David Wu^{1,2}, Joshua S. Catapano⁴, Kunal Raygor¹, Kazim Narsinh⁸, Helen Kim⁹, Shantel Weinsheimer⁹, Daniel L. Cooke^{3,8}, Brian P. Walcott¹⁰, Michael T. Lawton⁴, Nalin Gupta¹, Berislav V. Zlokovic^{11,12}, Edward F. Chang^{1,3}, Adib A. Abila^{1,3,*}, Daniel A. Lim^{1,2,3,13,*}, Tomasz J. Nowakowski^{1,2,3,5,6,14,*}

Cerebrovascular diseases are a leading cause of death and neurologic disability. Further understanding of disease mechanisms and therapeutic strategies requires a deeper knowledge of cerebrovascular cells in humans. We profiled transcriptomes of 181,388 cells to define a cell atlas of the adult human cerebrovasculature, including endothelial cell molecular signatures with arteriovenous segmentation and expanded perivascular cell diversity. By leveraging this reference, we investigated cellular and molecular perturbations in brain arteriovenous malformations, which are a leading cause of stroke in young people, and identified pathologic endothelial transformations with abnormal vascular patterning and the ontology of vascularly derived inflammation. We illustrate the interplay between vascular and immune cells that contributes to brain hemorrhage and catalog opportunities for targeting angiogenic and inflammatory programs in vascular malformations.

The cerebrovasculature comprises an uninterrupted, arborized network of vascular conduits through which circulating blood flows (1–3). It is tasked with ensuring delivery of oxygen, energy metabolites, and other nutrients to the brain while removing by-products of brain metabolism or preventing entry of circulating toxins (1, 3). Interruptions in cerebral blood flow or structural compromise and hemorrhage lead to stroke, which is a leading cause of death and disability worldwide (4, 5).

Like other vascular beds, the cerebrovasculature has functionally distinct, contiguous

segments identified as arteries, arterioles, capillaries, venules, and veins hierarchically organized along an “arteriovenous axis” (1, 6, 7). Cell composition varies with these transitions, and each cerebral vessel is composed of endothelial cells, pericytes, smooth muscle cells (SMCs), and/or perivascular fibroblast-like cells (referred to hereafter as perivascular fibroblasts) (1, 7, 8). Coordinated molecular interactions between vascular cells and surrounding neurons, glia, and perivascular immune cells endow the cerebrovasculature with medically relevant, specialized properties. The blood-brain barrier in capillaries, for example, provides a basis for brain immune privilege and serves as an obstacle to pharmacologic treatment of brain diseases (3, 6, 9–11).

Single-cell mRNA-sequencing (scRNA-seq) in mice has suggested additional cell variation and provided a molecular basis for arteriovenous phenotypic changes known as “zonations” (7, 12–14). Because of biases in cell isolation, existing human brain cell atlas studies have overlooked the cerebrovasculature, and its cellular heterogeneity has been largely unexplored in humans (15, 16). Neurologic diseases, such as stroke or Alzheimer’s disease, or brain aging show a predilection for select arteriovenous segments (12, 17–19). Thus, large-scale single-cell profiling of the human cerebrovasculature should provide a translational reference to better understand molecular underpinnings of selective cell vulnerabilities and patterns of aberrant gene expression in human cerebrovascular disease.

Cellular and molecular profiles of the adult human cerebrovasculature

To profile cells of the cerebrovasculature, we obtained normal cerebral cortex tissue from patients undergoing tailored lobectomies for epilepsy (table S1). Large arteries and veins were microdissected, and smaller vessels (arterioles, capillaries, and venules) were isolated by use of established methods (Fig. 1A and fig. S1A) (20–22). We processed for scRNA-seq dissociated cells from five individuals using the 10X Genomics Chromium platform and generated high-quality transcriptomes from 74,535 cells (fig. S1, B to E). We performed graph-based Leiden clustering, and clusters were annotated with differentially expressed genes to identify 15 major cell populations, each with a distinct set of enriched genes and present in multiple individuals (Fig. 1, B to D; fig. S1, F and G; and table S2).

On the basis of previously described gene expression patterns, we identified the major vascular cell classes: endothelial cells (*CLDN5*), pericytes (*KCNJ8*), SMCs (*MYH11*), and perivascular fibroblasts (*DCN*) (Fig. 1, B and C, and table S2) (7, 23, 24). Using our scRNA-seq analysis to inform probe design, we spatially resolved vascular cell diversity in the adult human cerebral cortex with multiplexed spatial transcriptomics (Fig. 2, A to D, and fig. S2, A to F). Consistent with known variations of the human cerebrovasculature, the spatial distribution of cerebrovascular cells revealed reduced vascular cell densities in the white matter (fig. S2A) (25). Cerebrovascular cell classes were organized in known vascular cytoarchitectural structures such as arteries, capillaries, and veins (Fig. 2D). Thus, we define cell classes across the major subdivisions of the cerebrovasculature by intersecting multiplexed spatial transcriptomics with cell-specific markers defined from scRNA-seq.

Endothelial diversity and arteriovenous zonation in humans

Endothelial cells compose the inner, blood-facing lining of the cerebrovasculature (1, 3). Identified by expression of *CLDN5* and *PECAMI1*, endothelial cells composed six clusters (Fig. 1, E and F). Using a previously annotated cell atlas of mouse endothelial cells (13), we found that gene expression signatures corresponding to four arteriovenous segments—arteries, capillaries, venules, and veins—consistently mapped onto distinct clusters in our dataset (Fig. 1, F and G; fig. S3, A to H; and table S3). We also identified three clusters of endothelial cells within the arterial zonation (Fig. 1, E and F, and fig. S3D), including a cluster enriched for *TXNIP*, a regulator of glucose metabolism and oxidative stress (26), likely representing a metabolic state of arterial endothelial cells. By visualizing the spatial position of endothelial arteriovenous zonation

¹Department of Neurological Surgery, University of California, San Francisco, CA, USA. ²Eli and Edythe Broad Center for Regeneration Medicine and Stem Cell Research, University of California, San Francisco, CA, USA. ³Weill Institute for Neurosciences, University of California, San Francisco, CA, USA. ⁴Department of Neurosurgery, Barrow Neurological Institute, Phoenix, AZ, USA. ⁵Department of Anatomy, University of California, San Francisco, CA, USA. ⁶Department of Psychiatry and Behavioral Sciences, University of California, San Francisco, CA, USA. ⁷Rebus Biosystems, Santa Clara, CA, USA. ⁸Department of Radiology and Biomedical Imaging, University of California, San Francisco, CA, USA. ⁹Center for Cerebrovascular Research, Department of Anesthesia and Perioperative Care, University of California, San Francisco, CA, USA. ¹⁰Department of Neurosurgery, NorthShore University HealthSystem, Evanston, IL, USA. ¹¹Department of Physiology and Neuroscience, Keck School of Medicine, University of Southern California, Los Angeles, CA, USA. ¹²Zilkha Neurogenetic Institute, Keck School of Medicine, University of Southern California, Los Angeles, CA, USA. ¹³San Francisco Veterans Affairs Medical Center, San Francisco, CA, USA. ¹⁴Chan Zuckerberg Biohub, San Francisco, CA, USA.

*Corresponding author. Email: adib.abila@ucsf.edu (A.A.A.); daniel.lim@ucsf.edu (D.A.L.); tomasz.j.nowakowski@gmail.com (T.J.N.)

†These authors contributed equally to this work.

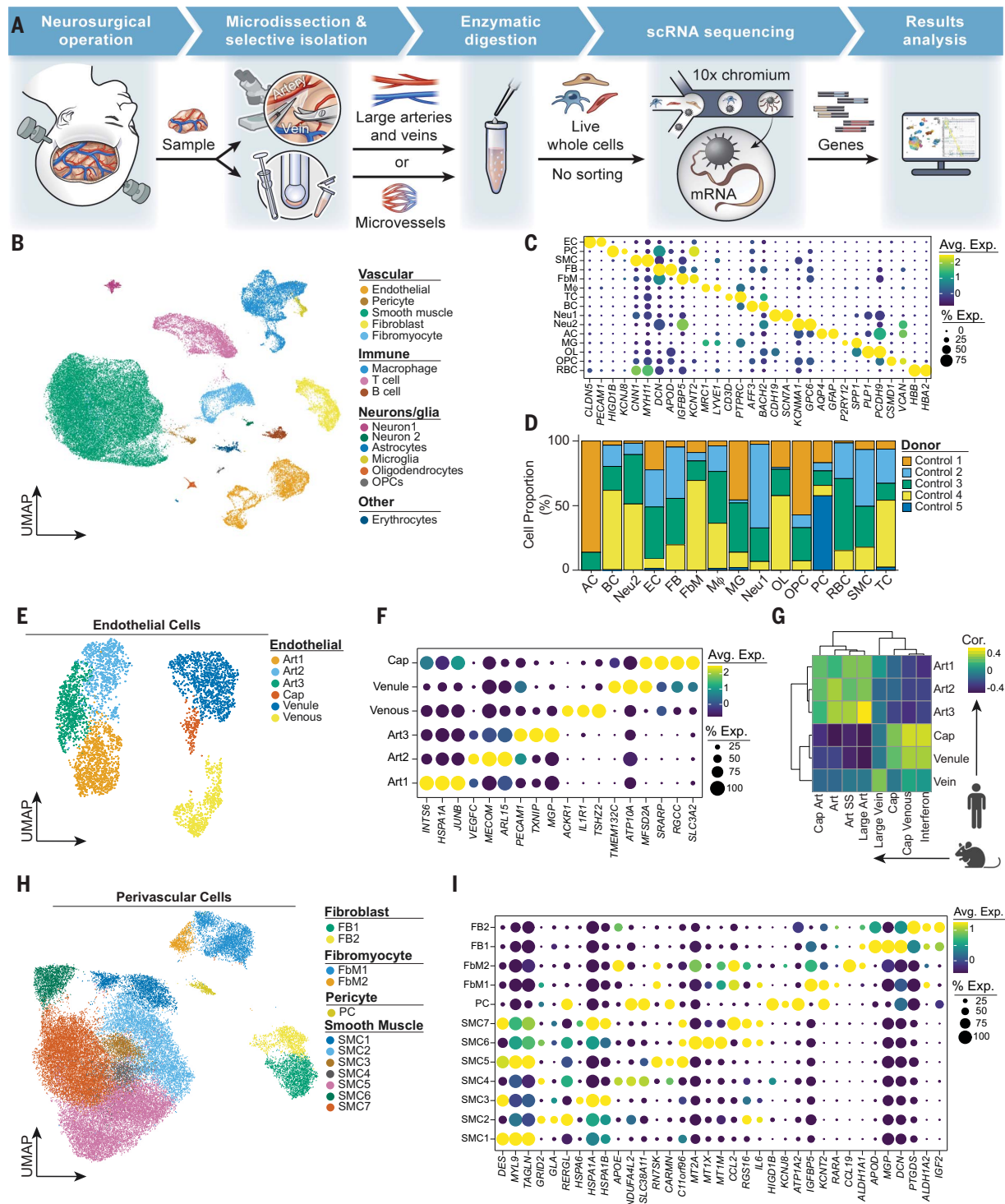


Fig. 1. Cells of the human cerebrovasculature. (A) Isolation and cell sampling from human cerebral cortex. scRNA, single cell mRNA. (B) UMAP visualization showing cell states from control adult cerebrovasculature ($n = 5$ donors). (C) Dot plot showing expression of cell state markers. EC, endothelial cell; PC, pericyte; SMC, smooth muscle cell; FB, perivascular fibroblast; FbM, fibromyocyte; M ϕ , macrophage; TC, T cell; BC, B cell; Neu, neuron; AC, astrocyte; MG, microglia; OL, oligodendrocyte; OPC, oligodendrocyte precursor cell; and RBC, erythrocyte. (D) Bar graph showing cell state proportion by donor. Number of cells sequenced by donor: control 1, 6033 cells; control 2, 25,730 cells; control 3, 22,816 cells;

control 4, 19,302 cells; and control 5, 654 cells. (E) UMAP visualization of endothelial cell states. Art, arterial; Cap, capillary. (F) Dot plot showing expression of endothelial cell state markers. (G) Correlation matrix of gene expression profiles between mouse and human cerebrovascular endothelial cell states. Mouse data obtained from a previously published database (13). Art, arterial; Cap, capillary; SS, shear stress. (H) UMAP visualization of perivascular cell states. FB, perivascular fibroblast; FbM, fibromyocyte; PC, pericyte; and SMC, smooth muscle cell. (I) Dot plot showing expression of perivascular cell state markers.

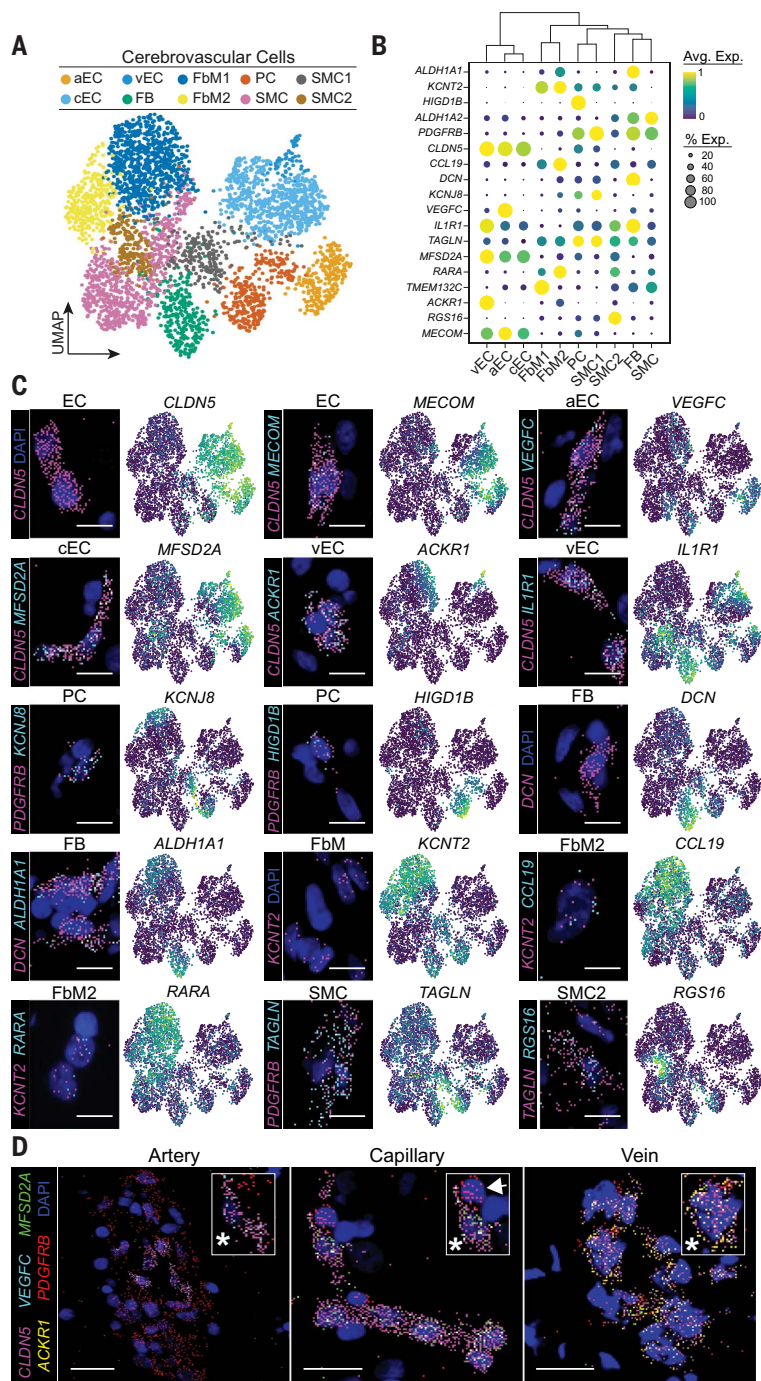


Fig. 2. Spatial RNA analysis resolves the cells of the human cerebrovasculature. (A) UMAP visualization of spatially defined cerebrovascular cell gene expression profiles identified by means of multiplexed, iterative single-molecule fluorescent in situ hybridization (smFISH). RNA molecules were quantified and assigned to cells through automated spot detection and nuclei segmentation. aEC, arterial endothelial cell; cEC, capillary endothelial cell; vEC, venous endothelial cell; FbM, fibrocyte; PC, pericyte; and SMC, smooth muscle cell. (B) Dot plot showing expression of cell state markers. (C) Representative high-magnification microscopy images of merged smFISH and expression distribution of cell state markers projected on UMAP embeddings from (A). DAPI (blue) stains are cell nuclei. Scale bar, 10 μ m. (D) Representative merged smFISH images showing cellular expression of *CLDN5* (magenta, endothelial cells), *VEGFC* (cyan, arterial endothelial cells), *MFSD2A* (green, capillary endothelial cells), *ACKR1* (yellow, venous endothelial cells), and *PDGFRB* (red, mural cells). DAPI (blue) stains are cell nuclei. (Left) Artery. Asterisk indicates endothelial cell coexpressing *CLDN5* (magenta) and *VEGFC* (cyan). Scale bar, 20 μ m. (Middle) Capillary. Asterisk indicates endothelial cell coexpressing *CLDN5* (magenta) and *MFSD2A* (green); arrow indicates *PDGFRB*-expressing pericyte (red). Scale bar, 15 μ m. (Right) Vein. Asterisk indicates endothelial cell coexpressing *CLDN5* (magenta) and *ACKR1* (yellow). Scale bar, 15 μ m.

markers and relationships with surrounding vascular cells, we confirmed *VEGFC*⁺, *MFSD2A*⁺, and *ACKR1*⁺ endothelium in arteries, capillaries, and veins, respectively (Fig. 2D) (7, 12, 13). Thus, our human vascular cell dataset captures the conserved distinctions of endothelial arteriovenous zonations in humans.

Diversity and distinction of brain perivascular cells

In addition to endothelial cells, we identified the major perivascular cell classes in the brain: pericytes, SMCs, and perivascular fibroblasts (Fig. 1, H and I; fig. S4, A to C; and table S2) (1, 7, 8). Our data serve as a reference for transcriptomic-based perivascular cell definitions on the basis of correlated patterns of gene expression variation (cell identity scores), as opposed to a handful of marker genes with partially overlapping patterns of expression (fig. S4, D to F) (8, 27, 28).

Pericytes are found in capillaries, venules, and some arterioles and induce and maintain the blood-brain barrier (20, 29, 30). Although previously identified pericyte markers, such as *ABCC9* and *KCNJ8*, together captured all putative pericyte clusters (Fig. 2, H and I; fig. S4G; and table S3) (7, 28), variations in their expression limited use of any single gene as a pan-pericyte marker. We therefore sought to nominate an alternative marker to capture a larger proportion of transcriptomically defined pericytes. Specifically, we identified that *HIGD1B* mRNA is highly enriched in pericytes and detected in 91.7% of pericytes (91.7% of cells, $\log_2FC = 3.10$, $P_{adj} < 0.01$) (Fig. 1I, fig. S4G, and table S2). We confirmed *HIGD1B* expression in *PDGFRB*⁺ or *KCNJ8*⁺ pericytes (Fig. 2, B and C).

SMCs are contractile cells in arteries, veins, and most arterioles (7, 31, 32). We selected these cells on the basis of expression of pan-SMC markers *CNN1*, *TAGLN*, and *MYH11* (Fig. 1, C and I, and fig. S3A). Iterative analysis of SMC transcriptional variation suggested that additional axes of variation may exist (Fig. 1, H and I, and table S3). For example, one cluster was enriched for metallothioneins *MTIX*, *MT2A*, *MT1M*, *MT1E*, and *MT1A*, which modulate SMC proliferation and migration (Fig. 2 and fig. S5A) (33). Additional transcriptional variation included the perivascular cell chemokine ligand *CCL2*, which coordinates brain response to systemic infection (Fig. 2 and fig. S5A) (34), and *RGS16*, which regulates sphingosine-1-phosphate signaling implicated in SMC proliferation (Figs. 2, B and C) (35). Thus, SMCs may represent a spectrum of transcriptional states, and future studies will be necessary to identify their functional roles.

Fibroblasts loosely adhere to arteries, arterioles, venules, and veins within the perivascular space, express extracellular matrix proteins, and provide structural support (7, 23, 36). We

identified two clusters of *DCN*⁺ and *APOD*⁺ perivascular fibroblasts (Fig. 1, H and I). None of the perivascular fibroblasts expressed markers of other brain fibroblasts—such as those in the meninges, which were surgically excluded in this study (37)—and *DCN*⁺ perivascular fibroblasts were visually confirmed to be associated with the cerebrovasculature (fig. S5B). Thus, our data confirm the presence of perivascular fibroblasts in the adult human brain.

Fibromyocytes in the human cerebrovasculature

Two cell clusters were not explained by known brain perivascular cell identities (Fig. 1, H and I, and fig. S4, D to F). We annotated these clusters as “fibromyocytes” on the basis of lower expression of contractile proteins (*TAGLN* and *ACTA2*) and higher expression of fibroblast (*DCN* and *LUM*) and macrophage (*LGALS3*) genes as described in peripheral arteries, such as the aorta and cervical internal carotid artery (38–40). No expression of the smooth muscle transcription factor *MYOCD* was detected, which suggests that fibromyocytes are distinct from SMCs (fig. S5C) (41). Differential gene expression identified *IGFBP5*, *KCNT2*, and *CCL19* to be more specific to fibromyocytes (fig. S5C and table S2), and we validated *KCNT2*⁺ and *CCL19*⁺ fibromyocytes in the human cerebral cortex (Fig. 2, A to C). Not identified in prior mouse cell atlases (7, 23, 24), our results demonstrate the presence of fibromyocytes in the human cerebrovasculature.

Fibromyocytes are thought to arise from SMCs in peripheral vascular beds (42). We therefore performed RNA velocity analysis, which infers transcriptomic trajectories according to the relative abundance of exonic and intronic reads (43). On the basis of inferred relationships of informatically predicted splicing dynamics, this analysis predicted that SMCs enriched for *CARMN*, a long noncoding RNA (lncRNA) associated with mesodermal differentiation (44), may give rise to fibromyocytes through the up-regulation of marker genes, such as *LGALS3*, *KCNT2*, and *IGFBP5* (fig. S5, D and E). However, in the absence of direct evidence of lineage tracing, we cannot conclusively demonstrate that such a relationship exists.

Retinoic acid signaling regulates smooth-muscle-to-fibromyocyte transitions in the periphery (39). However, prior human brain cell atlases have not documented nonmeningeal sources of retinoic acid (fig. S5F). Investigation of retinoic acid synthetic enzyme and receptor gene expression identified enrichment in brain fibromyocyte clusters and perivascular fibroblasts (Fig. 1I and fig. S5, G and H). We spatially confirmed *ALDH1A1* and *RARA* expression in *DCN*⁺ perivascular fibroblasts and *CCL19*⁺ fibromyocytes, respectively (Fig. 2, B and C). Thus, fibromyocytes and perivascular fibro-

blasts may be endogenous sources of retinoic acid in the adult human brain.

Deconstructing the dysplastic cerebrovasculature in arteriovenous malformations

To showcase the utility of our dataset, we generated a scRNA-seq dataset from arteriovenous malformation (AVM) samples (45). We obtained intraoperative, angiographically confirmed human brain AVMs from five patients (table S1). Using analogous dissection and scRNA-seq techniques (Fig. 3A), we generated high-quality whole-cell transcriptomes from 106,853 cells and identified 11 major cell populations (Fig. 3, B and C, and fig. S6, A to D). Each cell population was identified in multiple specimens, except for astrocytes and choroid plexus (Fig. 3C and fig. S6E). We spatially confirmed *CLDN5*⁺ endothelial cells, *TAGLN*⁺ SMCs, *CCL19*⁺ fibromyocytes, and *COL1A2*⁺ perivascular fibroblasts in AVMs (Fig. 3D). To identify endothelial and perivascular cell molecular changes in AVMs, we coembedded control and AVM scRNA-seq datasets (Fig. 3E and fig. S7A), identified differentially expressed genes (Fig. 3F; fig. S7, D to H; and table S4), and performed iterative clustering in each vascular cell class (Fig. 3E; figs. S8, A to E, and S9, A to C; and table S5). Thus, we define cell composition and cell-specific patterns of aberrant gene expression within AVMs.

Endothelial aberrancy in brain AVMs

AVMs arise from pathologic molecular changes in endothelial cells (46, 47). This catalyzes direct connections to form between arteries and veins without intervening capillaries and results in tortuous, dysmorphic tangles of blood vessels referred to as the “nidus” (45). Joint analysis of control and AVM datasets revealed that endothelial subsets were enriched for arterial and venous but not venular or capillary transcriptional identity scores in AVMs (Fig. 3, E and G, and fig. S9, D to G). Endothelial cell clusters with suppressed venule and capillary cell identities [nidus 1 (Nd1) and nidus 2 (Nd2)] showed greatest differential gene expression (Fig. 3H and table S6). RNA velocity analysis identified a consensus molecular trajectory from Nd1 to Nd2 (Fig. 3I and fig. S9H) and predicted a progressive up-regulation of *PLVAP*, a marker of fenestrated endothelium normally confined to developmental angiogenesis, the brain’s circumventricular organs and choroid plexus, and *PGF*, a potent stimulator of brain angiogenesis (Fig. 3I) (13, 30, 48, 49). Gene set enrichment analysis (GSEA) confirmed pathogenic cascades, such as angiogenesis, inflammation, and epithelial-to-mesenchymal transition, enriched in AVM Nd2 endothelium (Fig. 3J and table S7) (50–52). Control capillary endothelial cells robustly expressed blood-brain barrier nutrient trans-

porters, including *MFSD2A*, *SLC16A1*, and *SLC38A5* (Fig. 3K). By contrast, AVM Nd2 endothelial suppressed nutrient transporter expression and up-regulated pro-inflammatory (*CCL14*), pro-angiogenic (*PGF* and *STC1*), and pro-permeability (*PLVAP* and *ANGPT2*) genes (Fig. 3, K and L). Additionally, we confirmed the localization of Nd2 endothelial cells in the AVM nidus (Fig. 3M).

To characterize how pathologic endothelial gene expression may influence cell-to-cell communication networks, we used an in silico algorithm to predict reciprocal ligand-receptor interactions (53). The assembled interactome identified Nd2 as the strongest contributor to abnormal cell communications in AVMs (fig. S10A). Dysregulated communication pathways included established pathogenic cascades, such as angiopoietin, vascular endothelial growth factor, and transforming growth factor- β (TGF- β) signaling (54–56) as well as previously unrecognized immune activating and angiogenic communication networks in AVMs, such as *CD99*, *SPPI1*, and *CALCR* (fig. S10, B to F). Thus, aberrant nidus endothelial gene expression is predicted to result in pathologic cell-to-cell communication networks within AVMs.

Immune cell microenvironment and cerebrovascular-derived inflammation

Inflammation is hypothesized to play a role in the formation of AVMs (45, 52). Iterative analysis of the immune cell populations associated with the cerebrovasculature identified 17 immune cell clusters in coembedded cell populations (Fig. 4, A and B, and fig. S11, A and B). Nine clusters comprised myeloid cells, including vessel-associated microglia, conventional dendritic cells (cDCs), three perivascular macrophage (pvM ϕ) subpopulations, and three monocyte (Mo) subpopulations. In addition, we computationally separated myeloid cells with evidence of ex vivo activation (ExV) (Fig. 4, A and B, and fig. S11C) (57). Eight clusters comprised lymphoid cells, including CD4⁺ T cells, two CD8⁺ T cell subpopulations, regulatory T cells (T_{reg} cells), B cells, natural killer (NK) cells, plasmacytoid dendritic cells (pDCs), and a population of dividing lymphocytes (Div) composed of T_{reg} cells (Fig. 4, A and B). Resident pvM ϕ s were the most abundant immune cell population, composing 31.2% and 28.3% of immune cells in controls and AVMs, respectively (Fig. 4C). Greater than 90% of circulating immune cells, such as CD8⁺ T cells, were confined within the resting cerebrovasculature but infiltrated into the perivascular space or adjacent brain in AVMs ($P < 0.01$) (fig. S11, D and E).

Myeloid immune cells were more abundant and expressed gene signatures suggestive of activation in AVMs (Fig. 4, D to G, and fig. S11F), and we cataloged dysregulated immune cell communication networks

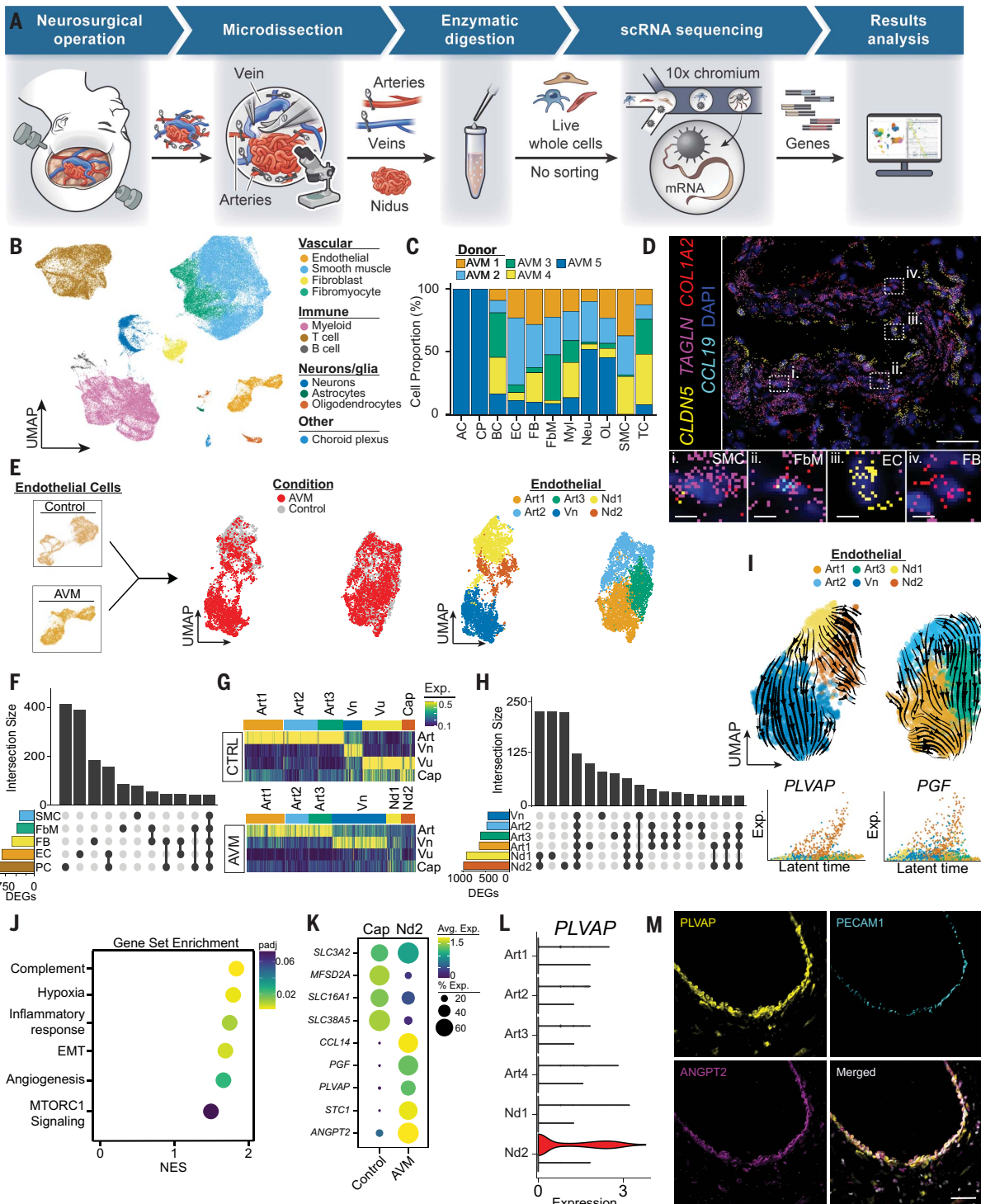


Fig. 3. Cellular aberrancy in the malformed cerebrovasculature. (A) Isolation and cell sampling from human brain AVMs. scRNA, single-cell mRNA. (B) UMAP visualization showing cell states from AVMs ($n = 5$ donors). (C) Bar graph showing cell state proportion by donor. Number of cells sequenced by donor are AVM1, 26,122 cells; AVM2, 28,868 cells; AVM3, 14,541 cells; AVM4, 26,660 cells; and AVM5, 10,662 cells. EC, endothelial cell; SMC, smooth muscle cell; FB, perivascular fibroblast; FbM, fibromyocyte; Myl, myeloid cells; TC, T cell; BC, B cell; Neu, neuron; AC, astrocyte; MG, microglia; OL, oligodendrocyte; and CP, choroid plexus. (D) Representative microscopy image of single-molecule fluorescent in situ hybridization showing expression of *CLDN5* [yellow, endothelial cells (EC)], *TAGLN*

[magenta, smooth muscle cells (SMC)], *COL1A2* [red, perivascular fibroblasts (FB)], and *CCL19* [cyan, fibromyocytes (FbM)]. DAPI (blue) stains are cell nuclei. Boxes highlight representative cells. Scale bar, 50 μm . (i) *TAGLN*⁺ smooth muscle cell. (ii) *CCL19*⁺ and *TAGLN*⁺ fibromyocyte. (iii) *CLDN5*⁺ endothelial cell. (iv) *COL1A2*⁺ perivascular fibroblast. Scale bars, insets, 5 μm . (E) (Left) Schematic describing computational pipeline. Endothelial cells (orange) are identified in silico by marker expression, coembedded for downstream analytics, and iteratively clustered. An identical workflow was applied to perivascular cells (fig. S7). (Middle) UMAP visualization of coembedded endothelial cell states in control (gray) and AVMs (red). (Right) UMAP visualization of iteratively clustered endothelial cell

states. Art, arterial; Cap, capillary; Vn, venous; and Nd, nidus. **(F)** Upset plot of DEGs (horizontal bars) by cell class. Number of DEGs exclusive to one cell class (black circles) or shared between multiple cell classes (linked black circles). Vertical bars show the number of genes per intersection. **(G)** Heatmap visualization of arteriovenous transcriptional identity in control (top, CTRL) and AVM (bottom) endothelial cell states. Art, arterial; Cap, capillary; Vu, venule; Vn, venous; Nd, nidus. Exp., expression; blue, low expression; and yellow, high expression. **(H)** Upset plot showing intersections of DEGs in AVM endothelial cell states compared with controls. **(I)** UMAP visualization of AVM endothelial cell RNA velocity reveals two divergent trajectories from Nd1

(fig. S11G). Vessel-associated CD11c⁺ antigen-presenting cells are potent activators of brain CD4⁺ T cell responses in situ (58, 59). scRNA-seq confirmed that vessel-associated CD11c⁺ cells were composed of myeloid cells, including cDCs, pMφs, and some microglia, and we identified a heterogeneous spatial distribution of vessel-associated antigen-presenting myeloid cells in the AVM nidus (Fig. 4F). Discrete areas appeared to have a greater number of IBA1⁺P2RY12⁻ macrophages or IBA1⁺P2RY12⁺ microglia, for example (Fig. 4, F and G). A pronounced perivascular myeloid cell response was observed, and IBA1⁺P2RY12⁻ macrophages were found at greater distances from the adjacent vasculature consistent with infiltration in AVMs ($P < 0.01$) (Fig. 4G). Thus, there are diverse cellular and spatially heterogeneous cerebrovascular inflammatory responses within AVMs.

Vascular immune cell cross-talk with brain hemorrhage

Hemorrhagic stroke is a devastating consequence of AVMs (60). We therefore sought to identify deleterious cell states associated with AVM rupture. We used scMappR to deconvolute cellular heterogeneity and to compute cell-specific gene expression signatures from AVM bulk RNA-seq ($n = 39$ AVMs; ruptured, 26 AVMs; unruptured, 13 AVMs) (Fig. 5A and table S1) (61). We first identified 871 differentially expressed genes (DEGs) associated with AVM rupture enriched in vascular developmental pathways (such as blood vessel development and morphogenesis) and inflammatory processes (such as cell recruitment) (fig. S12, A and B, and table S8). Using our scRNA-seq dataset, in silico cell abundance deconvolution resolved probable alterations in cell proportions (Fig. 5B). A subpopulation of *AIF1*⁺ (encodes IBA1)—*P2RY12*⁻ monocytes, identified as *GPNMB*⁺ Mo3 monocytes—was over-represented in ruptured AVMs ($P < 0.01$) and expressed gene signatures consistent with activation (Fig. 5, B to D, and fig. S12, C and D). Thus, distinct infiltrating immune cell states become enriched with AVM rupture.

Inflammation leads to a loss of vessel integrity, and SMCs contribute to brain hemorrhage when depleted (52, 62–64). In silico abundance of *GPNMB*⁺ monocytes and SMCs correlated

negatively in ruptured AVMs [correlation coefficient (r) = -0.43 , $P < 0.05$]. We therefore investigated whether *GPNMB*⁺ monocytes contribute to SMC death. Coculture of isolated *GPNMB*⁺ monocytes from ruptured AVM patients with primary brain vascular SMCs (VSMCs) increased apoptotic cleaved caspase-3⁺ VSMCs ($P < 0.01$) (Fig. 5E). Cell-to-cell communication analysis identified *SPPI* [which encodes osteopontin (OPN)] as the greatest dysregulated outgoing signaling pathway from *GPNMB*⁺ monocytes in AVMs (Fig. 5F). The ligand OPN is predicted and previously shown to interact with CD44 and integrin receptors on SMCs (65). Soluble OPN induced a 2.7-fold increase in VSMC apoptosis, which was ameliorated by pretreatment with neutralizing CD44 antibody, an integrin inhibitor, or a combination of both ($P < 0.01$) (Fig. 5G). Thus, *GPNMB*⁺ monocytes contribute to SMC depletion and are associated with AVM rupture and brain hemorrhage.

Discussion

We present a cell-resolution atlas that describes the transcriptomic heterogeneity underlying cell function and interaction in the human adult cerebrovasculature. We identified conservation of endothelial molecular zonation essential to arteriovenous phenotypic change and expanded cellular diversity of brain perivascular cells, including fibrocytes not previously identified in the cerebrovasculature (7, 23, 24). SMCs are predicted to transform into fibrocytes, but this will require validation with fate-tracing methods. Fibrocytes and perivascular fibroblasts may produce retinoic acid in the adult human brain. Retinoic acid signaling contributes to cortical vasculature development and modulates smooth muscle plasticity and fibrocyte speciation in other vascular beds (39, 66, 67). However, the functional relevance of these findings in the adult cerebrovasculature warrants further investigation.

This atlas has many implications for neuroscience and clinical medicine. To exemplify its utility, we defined cellular and gene expression changes in AVMs, a leading cause of stroke in young people, and identified pathologic endothelial molecular transformations, spatially localized to the AVM nidus. Some

(yellow). Up-regulation of *PLVAP* and *PGF* occurs with endothelial Nd1-to-Nd2 transitions. Exp., expression. **(J)** Gene set enrichment analysis of DEGs in AVM endothelial Nd2. P_{adj} , false discovery rate adjusted P value; NES, normalized enrichment score. **(K)** Dot plot showing top marker gene expression for control capillary and AVM Nd2 endothelial cells. Avg. Exp., average expression; Exp., expression **(L)** Violin plot of *PLVAP* expression showing specificity to AVM Nd2. **(M)** Representative confocal microscopy analysis of *PLVAP* (yellow) and *ANGPT2* (magenta) expression in PECAMI⁺ endothelial cells (cyan) in AVM nidus. Vessel shown in cross section. Colocalization of fluorescence results in white coloration. Scale bar, 50 μ m.

molecular changes are shared with immature embryonic endothelium or angiogenic tip cells, but other developmental or angiogenic transcriptional programs are notably absent or altered (14, 30, 68, 69). We also describe the cellular ontology and communication networks of cerebrovascular-derived inflammation. The interplay between vascular and immune cells, such as *GPNMB*⁺ monocytes and SMCs, induced pathological changes associated with brain hemorrhage. Consequently, our findings may guide the development of future therapies.

We recognize that this atlas represents only a first step toward a comprehensive census of the human cerebrovasculature. Limitations in unintended biases of cell capture or isolation and random sampling, such as relative proportions of small and large vessels from each individual, may alter relative cell proportions and require further validation in spatially resolved datasets. Additional work will also be needed to ascertain distinctions between cell types and cell states, such as transient or metabolic variations. Nonetheless, our results should inform future studies in other brain regions or cerebrovascular diseases to accelerate mechanistic understanding and therapeutic targeting of the human cerebrovasculature.

Materials and methods

Ethics statement and tissue acquisition

Human brain tissue specimens and clinical data were obtained from the University of California San Francisco with protocols approved from the institutional review board and ethics committee (IRB 10-01318 and 10-02012). All tissues were acquired from patients undergoing neurosurgical operations and written informed consent was obtained prior to the procedure permitting collection of tissue specimens for the purposes of research. Normal cerebral cortex was obtained as part of a neurosurgical operation to reach deep seated lesions causing epilepsy and uninvolved in the pathology. All specimens were >2 cm from any radiographic abnormality on magnetic resonance imaging, showed no abnormalities on routine electrocorticography, and were histologically normal on a rapid hematoxylin and eosin stain. Diagnosis of human brain AVMs

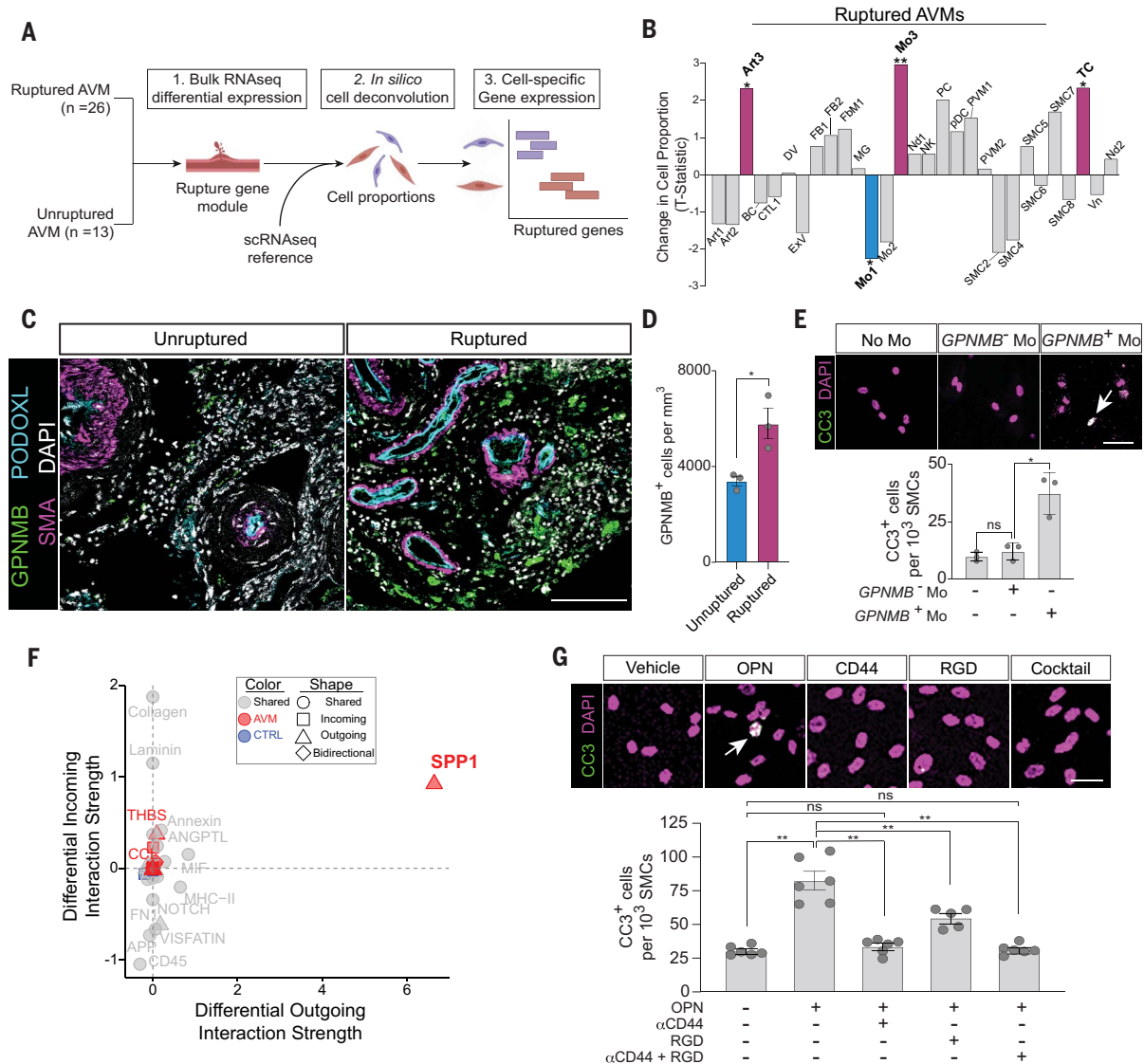


Fig. 5. Cell states implicated in brain AVM rupture. (A) Cellular deconvolution and cell-specific differential expression analysis of bulk RNA-seq from ruptured and unruptured brain AVM. (B) Bar graph of change in cell proportion *t* statistic in ruptured AVMs. Purple, increased cell abundance; blue, decreased cell abundance. **P* < 0.05; ***P* < 0.01. (C) Representative confocal microscopy imaging showing GPNMB⁺ monocytes (green), endothelial cells [cyan, podocalyxin (PODOXL)], and smooth muscle cells [magenta, α-smooth muscle actin (SMA)] in unruptured and ruptured AVMs. Scale bar, 100 μm. (D) Quantification of GPNMB⁺ monocytes in unruptured (blue) and ruptured (purple) AVMs (*n* = 3 donors per condition; three nonadjacent sections per donor; 8 to 10 random images per section). Mean ± SEM, two-tailed *t* test. **P* < 0.05. (E) (Top) Confocal microscopy analysis of cleaved caspase-3⁺ (green, CC3) human primary SMCs after coculture with GPNMB⁺ and GPNMB⁻ monocytes isolated from ruptured AVMs. DAPI (magenta) stains are cell nuclei. White, colocalization of CC3 and DAPI; arrow, CC3⁺ cell.

Scale bar, 20 μm. (Bottom) Quantification of CC3⁺ smooth muscle cells (*n* = 3 independent cultures per condition). Mo, monocytes. Mean ± SEM, ANOVA with Tukey post hoc test. **P* < 0.05; ns, not statistically significant. (F) Scatterplot of dysregulated cell communication pathways in AVM GPNMB⁺ monocytes (Mo3) relative to controls by scRNA-seq. Red, up-regulated in AVM; blue, up-regulated in control; gray, shared between conditions; triangle, outgoing network; square, incoming network; and diamond, outgoing and incoming network. (G) (Top) Confocal microscopy analysis of cleaved caspase-3⁺ (green, CC3) human primary smooth muscle cells treated with osteopontin (OPN, encoded by *SPP1*) and CD44-neutralizing antibody, RGD integrin inhibitor, or inhibitor cocktail. DAPI (magenta) stains are cell nuclei. White, colocalization of CC3 and DAPI; arrow, CC3⁺ cell. Scale bar, 20 μm. (Bottom) Quantification of CC3⁺ smooth muscle cells (*n* = 5 to 6 independent cultures per condition). Mo, monocytes. Mean ± SEM, ANOVA with Tukey post hoc test. ***P* < 0.01; ns, not statistically significant.

were angiographically confirmed preoperatively, and fresh tissues were acquired as part of planned surgical resection. For scRNA-seq, only unruptured brain AVMs were enrolled into the study. Specimen orientation was main-

tained to ensure coverage of arteriovenous axis with surgical clips of different sizes with aide of intraoperative fluorescent angiography. All tissues were acquired in close collaboration with neurosurgeons trained in tissue isolation

techniques to minimize tissue disruption such as avoidance of electrocautery. For bulk sequencing experiments, we utilized snap-frozen ruptured and unruptured AVM specimens as part of our biorepository. Patient demographic

information for all tissues utilized is summarized in table S1.

Isolation of cerebrovascular specimens

No differences in vascular isolation methods were applied between normal cerebral cortex or AVM tissues. Tissue specimens were placed in chilled preoxygenated Dulbecco's modified Eagle medium (DMEM, Fisher Scientific, Waltham, MA, catalog number: MT10017CV) and transported to the laboratory on ice. All tissue handling was performed with autoclave-sterilized equipment within a class II biological safety cabinet. Large arteries and veins were selectively isolated under $5\times$ magnification with a Leica MZ75 dissecting microscope (Leica Microsystems, Wetzlar, Germany) with two #5/45 Dumont micro-forceps (Fine Science Tools, Foster City, CA, catalog number: 11251-35). Under $5\times$ magnification, the lumen of each vessel was longitudinally opened with a #15 scalpel blade (Fine Science Tools) or flushed with DMEM. The large vessels were placed in an Eppendorf LoBind 5-ml tube (Eppendorf North America, Enfield, CT, catalog number: 0030122348) and kept on ice in chilled oxygenated DMEM. Following removal of all visible vasculature, the microvasculature was isolated using dextran gradient centrifugation followed by cell-strainer filtration (20–22). More specifically, tissue was cut into ~1- to 2-mm pieces with a scalpel and gently homogenized in a Dounce homogenizer containing oxygenated pre-chilled DMEM with 1% bovine serum albumin (BSA) (Sigma Aldrich, St. Louis, MO, catalog number: A9418). The homogenate was mixed in 18% dextran solution (MW: ~70,000 Da; Sigma-Aldrich, catalog number: 31390) at a volume ratio of 1:1 and centrifuged at 6000g for 20 min at 4°C. This resulted in a microvascular pellet and floating vascular-depleted brain. The floating vessel-depleted brain was gently aspirated and discarded. The vascular pellet resuspended in DMEM with 1% BSA and passed through a 40- μ m cell strainer (Fisher Scientific, catalog number: 08-771-1) to remove circulating cells or other debris. Microvascular fragments remain trapped on top of the cell strainer and were subsequently collected by inverting with cell strainer and washing with prechilled oxygenated DMEM. A small aliquot was visualized at 10X magnification to confirm both purity and yield with brightfield microscopy. The microvascular fragments were pelleted by centrifugation at 500g for 5 min. The supernatant was aspirated and then pooled with the microdissected arteries and veins from the same individual in prechilled oxygenated DMEM. These pooled preparations are referred to as isolated vascular preparations for subsequent steps and maintained in chilled oxygenated media on ice and immediately processed to create single-cell suspensions.

Generation of vascular single-cell suspensions

Isolated vascular preparations were incubated for 45 min in 0.2% collagenase type 2 (Worthington Biochemical Corporation, Lakewood, NJ, catalog number: LS004176) diluted in preoxygenated DMEM at 37°C with gentle agitation in an Eppendorf LoBind 5-ml tube (Eppendorf North America). Cell suspensions were filtered through a sterile 40- μ m cell strainer (Fisher Scientific) to isolate undigested debris. Cells contained within the flowthrough were collected by centrifugation at 500g at 5 min and the supernatant carefully aspirated. To lyse any residual erythrocytes, the cell pellet was resuspended in Gibco ACK lysing buffer (Fisher Scientific, catalog number: A1049201) for 3 min at room temperature. Cells were then collected by centrifugation at 500g at 5 min and washed three times with sterile RNase-free phosphate buffered saline (PBS) (Sigma-Aldrich, catalog number: D8537-500ml) containing 0.04% BSA. Cells were pelleted with centrifugation at 500g for 5 min and resuspended in PBS with 0.04% BSA. To confirm cell viability and yield, a 10- μ l aliquot of the cell suspension was mixed 1:1 with 0.4% trypan blue (Thermo Fisher Scientific, catalog number: T10282) to stain non-viable cells. Cells were then counted on a hemocytometer.

scRNA-seq

All scRNA-seq experiments were performed on freshly isolated, whole cells as described above. Droplet-based scRNA-seq was performed with 10X Genomics Chromium Single Cell 3 prime reagent kits v3 as described by the manufacturer (10X Genomics, Pleasanton, CA, product code: 1000092; $n = 5$ normal cortex samples and $n = 5$ AVMs). Based on hemocytometer counts, single cells were loaded onto chromium chips with a capture target of 15,000 cells per sample. When cell yield was sufficient, two reactions per individual were performed. Libraries were prepared following the provided manufacturer's protocol. Quality of prepared sequencing libraries were confirmed by electrophoretic analysis on an Agilent 4200 TapeStation System (Agilent Technologies, Santa Clara, CA). Libraries were sequenced with an Illumina NovaSeq 6000 (Illumina, San Diego, CA) with a targeted sequencing depth of 50,000 reads per cell.

Bulk RNA sequencing

Undigested, isolated vascular tissues from ruptured and unruptured AVMs were obtained from the operating room, snap frozen in liquid nitrogen and stored at -80°C . Snap frozen tissues were embedded in Optical Cutting Temperature Compound (Sakura Finetek USA, Torrance, CA, catalog number: 4583) and cryosectioned at a thickness of 20 μ m. Tissue scrolls were collected in RNAase free Eppendorf LoBind-1.5 ml microcentrifuge tubes

(Eppendorf North America, catalog number: 022431021). DNA/RNA Shield reagent (Zymo Research, Irvine, CA, catalog number: R1100) was added. Tissues were mechanically homogenized with a Squisher-Single homogenizer (Zymo Research, catalog number: H1001) and subsequently digested with proteinase K (Zymo Research, catalog number: R1057). Total RNA was isolated from the homogenized tissues with the Quick-RNA Miniprep Plus Kit as instructed by the manufacturer (Zymo Research, catalog number: R1057). The purified RNA was quantified with a NanoDrop (Thermo Fisher Scientific) and integrity confirmed with an Agilent 4200 TapeStation System (Agilent Technologies, Inc.). Ribosomal RNA was depleted using the NEBNext rRNA Depletion Kit as instructed by the manufacturer (New England Biolabs, Ipswich, MA, catalog number: E6310X), and sequencing libraries prepared with the SEQuoia Complete Stranded RNA Library Prep Kit (BioRad Laboratories, Hercules, CA, catalog number: 17005710). Sequencing library quality was confirmed on an Agilent 4200 TapeStation System (Agilent Technologies, Inc) and quantified with a Qubit dsDNA high sensitivity assay kit (Thermo Fisher Scientific). Libraries were sequenced in batch with an Illumina NovaSeq 6000 sequencer (Illumina) with targeted read depth of at least 5×10^7 reads per sample.

Rebus Esper spatial omics platform

Spatially resolved, multiplexed in situ RNA detection and analysis was performed using the automated Rebus Esper spatial omics platform (Rebus Biosystems, Santa Clara, CA). By intersecting a list of known or candidate cell type markers generated by scRNA-seq, suitability for probe design, including gene length and relative abundance, and design constraints for compatibility with the Rebus Esper spatial omics platform using proprietary software, we generated the following gene probe panel: *MECOM*, *RGS16*, *RARA*, *MFS2A*, *TAGLN*, *IL1R1*, *VEGFC*, *KCNJ8*, *DCN*, *TMEM132C*, *CCL19*, *CLDN5*, *PDGFRB*, *HIGD1B*, *KCNT2*, *ALDH1A2*, and *ALDH1A1*. Experiments and analyses using the Rebus Esper spatial omics platform were performed as previously described (70).

Immunofluorescent staining of tissues and cerebrovascular fragments

Formalin-fixed paraffin-embedded tissue sections were cut at a thickness of 6 μ m, deparaffinized with xylene, and rehydrated to distilled water with serial ethanol washes. For immunostaining of isolated vessel fragments, cerebrovascular vessel isolation was performed as described above and immersion fixed in 4% paraformaldehyde overnight at 4°C. For antigen retrieval, all specimens were incubated with pH 9 Tris-EDTA buffer at 97°C for 15 min. Tissue sections were then blocked with PBS

containing 0.2% gelatin, 1% donkey serum, and 1% triton for 1 hour at room temperature and incubated in the following primary antibodies overnight at 4°C. Primary antibodies included: podocalyxin (1:100, R&D Systems, Minneapolis, MN, catalog number: AF1658), alpha smooth muscle actin clone 1A4 (1:100, Dako North America, Inc. Carpinteria, CA, catalog number: M085129), P2RY12 (1:500, Sigma Aldrich, catalog number: HPA014518), IBA1 (1:500, Synaptic Systems, Goettingen, Germany, catalog number: 234004), PECAMI (1:50, Agilent Technologies, catalog number: M0882329), PLVAP (1:100, Sigma Aldrich, catalog number: HPA002279), angiotensin-2 (1:100, R&D systems, catalog number: AF623), PDGFRB (28E1) (1:100, Cell Signaling Technology, catalog number: 3169S), GPNMB (1:100, R&D systems, catalog number: AF2550), and CD8 clone C8/144B (1:100, Dako North America, catalog number: M710301). Sections were washed with PBS containing 1% Triton and incubated with fluorescent dye-conjugated secondary antibodies for 2 hours at room temperature. Alexa Fluor 488-conjugated donkey anti-mouse secondary antibody (1:500, Thermo Scientific, catalog number: A32766), Alexa Fluor 546-conjugated donkey anti-rabbit secondary antibody (1:500, Thermo Fisher, catalog number: A10040), and Alexa Fluor 647-conjugated donkey anti-goat secondary antibodies (1:500, Thermo Fisher, catalog number: A32787) were used to detect mouse, rabbit, and goat primary antibodies, respectively. Sections were washed and autofluorescence quenched by incubating with 1% Sudan Black (Sigma Aldrich, catalog number: 199664) for 10 min at room temperature. Slides were mounted with 4-prime,6-diamidino-2-phenylindole (DAPI)-containing Fluoromount-G (SouthernBiotech, Birmingham, AL, catalog number: 0100-20). All imaging was performed with a Leica TCS SP8 X confocal microscope with a 20X objective (Leica Microsystems).

Fluorescence-activated cell sorting (FACS)

To isolate circulating GPNMB⁺ and GPNMB⁻ monocytes, 10 ml of whole blood was collected in standard 5-ml EDTA-containing vacutainer blood collection tubes obtained from adult patients with acutely ruptured AVMs. Cells were subsequently centrifuged at 500g for 5 min and erythrocytes were then lysed with incubation in Gibco ACK lysing buffer (Fisher Scientific, catalog number: A1049201). The resulting cell suspension was filtered through a sterile 40-µm filter to remove debris and washed with PBS containing 0.04% BSA. Cell suspensions were then resuspended in FACS staining buffer (Thermo Fisher Scientific, catalog number: 00-4222-26). Cells were blocked to prevent non-specific staining, and cells were stained with Alexa Fluor 647-conjugated mouse anti-human CD45 monoclonal anti-

body clone HI30 (1.25 ng/µl, Thermo Fisher Scientific, catalog number: 51-0459-42), FITC-conjugated mouse anti-human CD11b monoclonal antibody clone ICRF44 (5.0 ng/µl, Thermo Fisher Scientific, catalog number: 11-0118-42), and PE-conjugated mouse anti-human GPNMB monoclonal antibody clone HOST5DS (1.25 ng/µl, Thermo Fisher Scientific, catalog number: 12-9838-42) for 30 min at room temperature. Cells were subsequently isolated by FACS with a BD FACSAria II Flow Cytometer (BD Biosciences, Franklin Lakes, NJ). Viable CD45⁺CD11b⁺GPNMB⁺ cells and CD45⁺CD11b⁺GPNMB⁻ cells were separately collected for subsequent coculture experiments.

Cell culture

All cell culture experiments utilized primary human brain vascular smooth muscle cells (VSMCs, ScienCell Research Laboratories, Carlsbad, CA, catalog number: 1100). Cells were cultured in SMC media in 5% CO₂ at 37°C. Early passage (P3, P4) cultures were used in the present study. Primary VSMCs were plated in equal number for all conditions. VSMCs were grown on 96-well tissue culture plates pre-coated with collagen. For coculture experiments, CD45⁺CD11b⁺GPNMB⁺ or CD45⁺CD11b⁺GPNMB⁻ cells were immediately cocultured with VSMCs following FACS isolation at an approximate ratio of 1:1 (71). Monocytes and VSMCs were cocultured for 24 hours and then subsequently fixed with 4% paraformaldehyde for subsequent immunostaining. For osteopontin (OPN, encoded by *SPP1*) treatment studies, cells were pretreated with vehicle control or anti-human CD44 neutralizing monoclonal antibody (10 µg/ml, Thermo Fisher Scientific, catalog number: MA4400), RGD peptide to inhibit integrin receptors (10 µM, Sigma Aldrich, catalog number: A8052), or both in combination for 30 min as previously described (65). Cultures were then subsequently treated with OPN (200 ng/ml, Sigma Aldrich, catalog number: SRP3131) for 6 hours. The cell culture media was changed and cells were then fixed with 4% paraformaldehyde for subsequent immunostaining.

Cell culture immunostaining

Paraformaldehyde fixed cells were blocked with PBS containing 0.2% gelatin, 1% donkey serum, and 0.1% triton for 1 hour at room temperature and incubated in primary antibodies overnight at 4°C. Primary antibodies included: alpha smooth muscle actin clone 1A4 (1:100, Dako North America, Carpinteria, CA, catalog number: M085129) and cleaved caspase-3 (1:300, Cell Signaling, catalog number: 9661S). Alexa Fluor 488-conjugated donkey anti-mouse secondary antibody (1:500, Thermo Scientific, catalog number: A32766) and Alexa Fluor 546-conjugated donkey anti-rabbit secondary

antibody (1:500, Thermo Fisher, catalog number: A10040) were used to detect mouse and rabbit primary antibodies, respectively. Cells were washed and nuclei stained with DAPI. All imaging was performed with a Leica TCS SP8 X confocal microscope with a 20X objective (Leica Microsystems, Inc.).

Tissue and cell culture image analysis

For all quantitative imaging experiments, a tile-scan image was generated encompassing the tissue section or cell culture well with 10- to 12-µm z-stack and maximum projection z-stack images were reconstructed. For all tissue studies, 8 to 10 randomly selected fields in three non-adjacent tissue sections per tissue specimen were analyzed as previously described (20). Tissues from three donors per condition were used for all analyses. For quantification of IBA1⁺, P2RY12⁺, and CD8⁺ immune cells, cell bodies were counted with the NIH ImageJ multipoint tool and expressed as number of positive cells per cubic millimeter of tissue. For immune cell distance analysis, the distance between cell bodies and abluminal vascular wall was measured using the NIH ImageJ length measurement tool. For coculture experiments, three independent cultures were analyzed per condition. For OPN experiments, 5 to 6 independent cultures were analyzed per condition. Cleaved caspase-3⁺ cells were counted with the NIH ImageJ multipoint tool, normalized to total cell number, and expressed per 1000 SMCs.

Single-cell RNA-sequencing analysis

Salmon Alevin 1.3.0 was used to create a cell by gene matrix for spliced and unspliced counts using the annotation from GENCODE 34 for GRCh38 (72, 73). Solo was used for doublet detection and removal and enriched softmax values in clusters were used as additional criteria for another round of doublet filtering (74). A minimum of 1000 genes and 40% mitochondrial cutoff were used to remove low quality cells from all datasets. The SCTransform workflow was used for count normalization (75). Principal component analysis was computed on the residuals for input into Harmony for batch correction (76). Control immune cells were not batch corrected due to inability to resolve rare cell types after correction. The parameters of Harmony were set to use the top 30 principal components. Uniform manifold approximation and projection (UMAP) embeddings and neighbors for Leiden clustering used the batch corrected embeddings (77, 78). RNA velocity analysis was done using the scVelo package (79). HGNC labels replaced all corresponding Ensembl gene ID and non HGNC annotated gene IDs were left in the matrix as Ensembl gene IDs. Latent time from scVelo was computed to order the cells. RNA velocity analysis was performed on batch

corrected embeddings. dittoSeq was used for color-blind friendly plotting (80). CellChat was used to infer cell communication analysis (53). scMappR was used to deconvolute gene expression between bulk gene expression datasets using the AVM perivascular, endothelial, and immune cell types as the reference (61). Correlations between mouse and human endothelial cell types were calculated on the space of shared orthologous marker genes of clusters. fgsea was used to look for enriched hallmark pathways from differential expressed endothelial genes (81). The *t* statistic for cell type proportions was based on deconvolution output from scMappR. All marker genes were using a Wilcoxon rank-sum test with a minimum of 0.5 average log fold-change cutoff and filtering for genes with <0.05 FDR with Bonferroni correction. UCell was used for the cell type identity score and utilized the top 30 genes of the cluster (82). More specifically, gene lists were generated using a Wilcoxon rank sum test and filtered for statistical significance (FDR < 0.01) for the top 30 genes. For endothelial cells, this list was also intersected with published mouse datasets based on their specificity after aggregating into four different subclasses: artery, capillary, venule, and vein (13). Genes used for UCell scoring for each cell type are listed in table S10.

Spatial transcriptomic analysis

The RNA spot table was log-normalized and scaled before PCA. The top 10 components were used for UMAP and neighbor analysis for Leiden clustering using the scanpy package.

Bulk tissue RNA-sequencing analysis

Salmon 1.3.0 was used to pseudo-align all ruptured and unruptured bulk AVM samples (83). The output of Salmon was used to generate counts using tximport (84). edgeR was used to compute differential gene expression between rupture and unruptured samples using the exact test (85). Genes with a false discovery rate (FDR)-adjusted *q* value < 0.05 were considered to be differentially expressed.

Statistical analysis

For all immunostaining and cell culture experiments, statistical analysis was performed with Student's *t* test for two-way comparisons and one-way analysis of variance (ANOVA) with post hoc Tukey tests for comparisons of three or more groups using GraphPad Prism. Data are presented as mean ± standard error of the mean unless otherwise indicated with individual data points shown.

Schematics

Schematic cartoons in Fig. 5A were created with BioRender.com.

REFERENCES AND NOTES

- S. Schaeffer, C. Iadecola, Revisiting the neurovascular unit. *Nat. Neurosci.* **24**, 1198–1209 (2021). doi: [10.1038/s41593-021-00904-7](https://doi.org/10.1038/s41593-021-00904-7); pmid: [34354283](https://pubmed.ncbi.nlm.nih.gov/34354283/)
- M. D. Sweeney, K. Kisler, A. Montagne, A. W. Toga, B. V. Zlokovic, The role of brain vasculature in neurodegenerative disorders. *Nat. Neurosci.* **21**, 1318–1331 (2018). doi: [10.1038/s41593-018-0234-x](https://doi.org/10.1038/s41593-018-0234-x); pmid: [30250261](https://pubmed.ncbi.nlm.nih.gov/30250261/)
- M. D. Sweeney, Z. Zhao, A. Montagne, A. R. Nelson, B. V. Zlokovic, Blood-brain barrier: From physiology to disease and back. *Physiol. Rev.* **99**, 21–78 (2019). doi: [10.1152/physrev.00050.2017](https://doi.org/10.1152/physrev.00050.2017); pmid: [30280653](https://pubmed.ncbi.nlm.nih.gov/30280653/)
- GBD 2016 Lifetime Risk of Stroke Collaborators, Global, regional, and country-specific lifetime risks of stroke, 1990 and 2016. *N. Engl. J. Med.* **379**, 2429–2437 (2018). doi: [10.1056/NEJMoal804492](https://doi.org/10.1056/NEJMoal804492); pmid: [30575491](https://pubmed.ncbi.nlm.nih.gov/30575491/)
- GBD 2016 Stroke Collaborators, Global, regional, and national burden of stroke, 1990–2016: A systematic analysis for the Global Burden of Disease Study 2016. *Lancet Neurol.* **18**, 439–458 (2019). doi: [10.1016/S1474-4422\(19\)30034-1](https://doi.org/10.1016/S1474-4422(19)30034-1); pmid: [30871944](https://pubmed.ncbi.nlm.nih.gov/30871944/)
- R. Daneman, A. Prat, The blood-brain barrier. *Cold Spring Harb. Perspect. Biol.* **7**, a020412 (2015). doi: [10.1101/cshperspect.a020412](https://doi.org/10.1101/cshperspect.a020412); pmid: [25561720](https://pubmed.ncbi.nlm.nih.gov/25561720/)
- M. Vanlandewijck et al., A molecular atlas of cell types and zonation in the brain vasculature. *Nature* **554**, 475–480 (2018). doi: [10.1038/nature25739](https://doi.org/10.1038/nature25739); pmid: [29443965](https://pubmed.ncbi.nlm.nih.gov/29443965/)
- J. M. Ross et al., The expanding cell diversity of the brain vasculature. *Front. Physiol.* **11**, 600767 (2020). doi: [10.3389/fphys.2020.600767](https://doi.org/10.3389/fphys.2020.600767); pmid: [33343397](https://pubmed.ncbi.nlm.nih.gov/33343397/)
- J. V. Forrester, P. G. McMenamin, S. J. Dando, CNS infection and immune privilege. *Nat. Rev. Neurosci.* **19**, 655–671 (2018). doi: [10.1038/s41583-018-0070-8](https://doi.org/10.1038/s41583-018-0070-8); pmid: [30310148](https://pubmed.ncbi.nlm.nih.gov/30310148/)
- W. M. Partridge, Blood-brain barrier and delivery of protein and gene therapeutics to brain. *Front. Aging Neurosci.* **11**, 373 (2020). doi: [10.3389/fnagi.2019.00373](https://doi.org/10.3389/fnagi.2019.00373); pmid: [31998120](https://pubmed.ncbi.nlm.nih.gov/31998120/)
- Z. Zhao, A. R. Nelson, C. Betsholtz, B. V. Zlokovic, Establishment and dysfunction of the blood-brain barrier. *Cell* **163**, 1064–1078 (2015). doi: [10.1016/j.cell.2015.10.067](https://doi.org/10.1016/j.cell.2015.10.067); pmid: [26590417](https://pubmed.ncbi.nlm.nih.gov/26590417/)
- M. B. Chen et al., Brain endothelial cells are exquisite sensors of age-related circulatory cues. *Cell Rep.* **30**, 4418–4432.e4 (2020). doi: [10.1016/j.celrep.2020.03.012](https://doi.org/10.1016/j.celrep.2020.03.012); pmid: [32234477](https://pubmed.ncbi.nlm.nih.gov/32234477/)
- J. Kalucka et al., Single-cell transcriptome atlas of murine endothelial cells. *Cell* **180**, 764–779.e20 (2020). doi: [10.1016/j.cell.2020.01.015](https://doi.org/10.1016/j.cell.2020.01.015); pmid: [32059779](https://pubmed.ncbi.nlm.nih.gov/32059779/)
- M. F. Sabbagh et al., Transcriptional and epigenomic landscapes of CNS and non-CNS vascular endothelial cells. *eLife* **7**, e36187 (2018). doi: [10.7554/eLife.36187](https://doi.org/10.7554/eLife.36187); pmid: [30188322](https://pubmed.ncbi.nlm.nih.gov/30188322/)
- R. D. Hodge et al., Conserved cell types with divergent features in human versus mouse cortex. *Nature* **573**, 61–68 (2019). doi: [10.1038/s41586-019-1506-7](https://doi.org/10.1038/s41586-019-1506-7); pmid: [31435019](https://pubmed.ncbi.nlm.nih.gov/31435019/)
- T. J. Nowakowski et al., Spatiotemporal gene expression trajectories reveal developmental hierarchies of the human cortex. *Science* **358**, 1318–1323 (2017). doi: [10.1126/science.aap8809](https://doi.org/10.1126/science.aap8809); pmid: [29217575](https://pubmed.ncbi.nlm.nih.gov/29217575/)
- A. Montagne et al., APOE4 leads to blood-brain barrier dysfunction predicting cognitive decline. *Nature* **581**, 71–76 (2020). doi: [10.1038/s41586-020-2247-3](https://doi.org/10.1038/s41586-020-2247-3); pmid: [32376954](https://pubmed.ncbi.nlm.nih.gov/32376954/)
- D. A. Nation et al., Blood-brain barrier breakdown is an early biomarker of human cognitive dysfunction. *Nat. Med.* **25**, 270–276 (2019). doi: [10.1038/s41591-018-0297-y](https://doi.org/10.1038/s41591-018-0297-y); pmid: [30643288](https://pubmed.ncbi.nlm.nih.gov/30643288/)
- J. Ratelade et al., Reducing hypermuscularization of the transitional segment between arterioles and capillaries protects against spontaneous intracerebral hemorrhage. *Circulation* **141**, 2078–2094 (2020). doi: [10.1161/CIRCULATIONAHA.119.040963](https://doi.org/10.1161/CIRCULATIONAHA.119.040963); pmid: [32183562](https://pubmed.ncbi.nlm.nih.gov/32183562/)
- R. D. Bell et al., Pericytes control key neurovascular functions and neuronal phenotype in the adult brain and during brain aging. *Neuron* **68**, 409–427 (2010). doi: [10.1016/j.neuron.2010.09.043](https://doi.org/10.1016/j.neuron.2010.09.043); pmid: [21040844](https://pubmed.ncbi.nlm.nih.gov/21040844/)
- E. A. Winkler, J. D. Sengillo, R. D. Bell, J. Wang, B. V. Zlokovic, Blood-spinal cord barrier pericyte reductions contribute to increased capillary permeability. *J. Cereb. Blood Flow Metab.* **32**, 1841–1852 (2012). doi: [10.1038/jcbfm.2012.113](https://doi.org/10.1038/jcbfm.2012.113); pmid: [22850407](https://pubmed.ncbi.nlm.nih.gov/22850407/)
- Z. Zhao et al., Central role for PICALM in amyloid- β blood-brain barrier transcytosis and clearance. *Nat. Neurosci.* **18**, 978–987 (2015). doi: [10.1038/nn.4025](https://doi.org/10.1038/nn.4025); pmid: [26005850](https://pubmed.ncbi.nlm.nih.gov/26005850/)
- A. Saunders et al., Molecular diversity and specializations among the cells of the adult mouse brain. *Cell* **174**, 1015–1030.e16 (2018). doi: [10.1016/j.cell.2018.07.028](https://doi.org/10.1016/j.cell.2018.07.028); pmid: [30096299](https://pubmed.ncbi.nlm.nih.gov/30096299/)
- A. Zeisel et al., Molecular architecture of the mouse nervous system. *Cell* **174**, 999–1014.e22 (2018). doi: [10.1016/j.cell.2018.06.021](https://doi.org/10.1016/j.cell.2018.06.021); pmid: [30096314](https://pubmed.ncbi.nlm.nih.gov/30096314/)
- T. Kubiková, P. Kochová, P. Tomášek, K. Witter, Z. Tonar, Numerical and length densities of microvessels in the human brain: Correlation with preferential orientation of microvessels in the cerebral cortex, subcortical grey matter and white matter, pons and cerebellum. *J. Chem. Neuroanat.* **88**, 22–32 (2018). doi: [10.1016/j.jchemneu.2017.11.005](https://doi.org/10.1016/j.jchemneu.2017.11.005); pmid: [29113946](https://pubmed.ncbi.nlm.nih.gov/29113946/)
- X. Li et al., Thioredoxin-interacting protein promotes high-glucose-induced macrovascular endothelial dysfunction. *Biochem. Biophys. Res. Commun.* **493**, 291–297 (2017). doi: [10.1016/j.bbrc.2017.09.028](https://doi.org/10.1016/j.bbrc.2017.09.028); pmid: [28890350](https://pubmed.ncbi.nlm.nih.gov/28890350/)
- A. Armulik, G. Genové, C. Betsholtz, Pericytes: Developmental, physiological, and pathological perspectives, problems, and promises. *Dev. Cell* **21**, 193–215 (2011). doi: [10.1016/j.devcel.2011.07.001](https://doi.org/10.1016/j.devcel.2011.07.001); pmid: [21839917](https://pubmed.ncbi.nlm.nih.gov/21839917/)
- L. He et al., Analysis of the brain mural cell transcriptome. *Sci. Rep.* **6**, 35108 (2016). doi: [10.1038/srep35108](https://doi.org/10.1038/srep35108); pmid: [27725773](https://pubmed.ncbi.nlm.nih.gov/27725773/)
- A. Armulik et al., Pericytes regulate the blood-brain barrier. *Nature* **468**, 557–561 (2010). doi: [10.1038/nature09522](https://doi.org/10.1038/nature09522); pmid: [20944627](https://pubmed.ncbi.nlm.nih.gov/20944627/)
- R. Daneman, L. Zhou, A. A. Kebede, B. A. Barres, Pericytes are required for blood-brain barrier integrity during embryogenesis. *Nature* **468**, 562–566 (2010). doi: [10.1038/nature09513](https://doi.org/10.1038/nature09513); pmid: [20944625](https://pubmed.ncbi.nlm.nih.gov/20944625/)
- R. A. Hill et al., Regional blood flow in the normal and ischemic brain is controlled by arteriolar smooth muscle cell contractility and not by capillary pericytes. *Neuron* **87**, 95–110 (2015). doi: [10.1016/j.neuron.2015.06.001](https://doi.org/10.1016/j.neuron.2015.06.001); pmid: [26119027](https://pubmed.ncbi.nlm.nih.gov/26119027/)
- L. C. D. Smyth et al., Markers for human brain pericytes and smooth muscle cells. *J. Chem. Neuroanat.* **92**, 48–60 (2018). doi: [10.1016/j.jchemneu.2018.06.001](https://doi.org/10.1016/j.jchemneu.2018.06.001); pmid: [29885791](https://pubmed.ncbi.nlm.nih.gov/29885791/)
- S. Zbinden et al., Metallothionein enhances angiogenesis and arteriogenesis by modulating smooth muscle cell and macrophage function. *Arterioscler. Thromb. Vasc. Biol.* **30**, 477–482 (2010). doi: [10.1161/ATVBAHA.109.200949](https://doi.org/10.1161/ATVBAHA.109.200949); pmid: [20056912](https://pubmed.ncbi.nlm.nih.gov/20056912/)
- L. Duan et al., PDGFR β cells rapidly relay inflammatory signal from the circulatory system to neurons via chemokine CCL2. *Neuron* **100**, 183–200.e8 (2018). doi: [10.1016/j.neuron.2018.08.030](https://doi.org/10.1016/j.neuron.2018.08.030); pmid: [30269986](https://pubmed.ncbi.nlm.nih.gov/30269986/)
- M. C. Hendriks-Balk et al., Sphingosine-1-phosphate regulates RGS2 and RGS16 mRNA expression in vascular smooth muscle cells. *Eur. J. Pharmacol.* **606**, 25–31 (2009). doi: [10.1016/j.ejphar.2009.01.018](https://doi.org/10.1016/j.ejphar.2009.01.018); pmid: [19374869](https://pubmed.ncbi.nlm.nih.gov/19374869/)
- A. M. Rajan, R. C. Ma, K. M. Kocha, D. J. Zhang, P. Huang, Dual function of perivascular fibroblasts in vascular stabilization in zebrafish. *PLoS Genet.* **16**, e1008800 (2020). doi: [10.1371/journal.pgen.1008800](https://doi.org/10.1371/journal.pgen.1008800); pmid: [33108800](https://pubmed.ncbi.nlm.nih.gov/33108800/)
- J. DeSisto et al., Single-cell transcriptomic analyses of the developing meninges reveal meningeal fibroblast diversity and function. *Dev. Cell* **54**, 43–59.e4 (2020). doi: [10.1016/j.devcel.2020.06.009](https://doi.org/10.1016/j.devcel.2020.06.009); pmid: [32634398](https://pubmed.ncbi.nlm.nih.gov/32634398/)
- Y. Li et al., Single-cell transcriptome analysis reveals dynamic cell populations and differential gene expression patterns in control and aneurysmal human aortic tissue. *Circulation* **142**, 1374–1388 (2020). doi: [10.1161/CIRCULATIONAHA.120.046528](https://doi.org/10.1161/CIRCULATIONAHA.120.046528); pmid: [33017217](https://pubmed.ncbi.nlm.nih.gov/33017217/)
- H. Pan et al., Single-cell genomics reveals a novel cell state during smooth muscle cell phenotypic switching and potential therapeutic targets for atherosclerosis in mouse and human. *Circulation* **142**, 2060–2075 (2020). doi: [10.1161/CIRCULATIONAHA.120.048378](https://doi.org/10.1161/CIRCULATIONAHA.120.048378); pmid: [32962412](https://pubmed.ncbi.nlm.nih.gov/32962412/)
- R. C. Wirka et al., Atheroprotective roles of smooth muscle cell phenotypic modulation and the TCF21 disease gene as revealed by single-cell analysis. *Nat. Med.* **25**, 1280–1289 (2019). doi: [10.1038/s41591-019-0512-5](https://doi.org/10.1038/s41591-019-0512-5); pmid: [31359001](https://pubmed.ncbi.nlm.nih.gov/31359001/)
- X. Long, R. D. Bell, W. T. Gerthoffer, B. V. Zlokovic, J. M. Miano, Myocardin is sufficient for a smooth muscle-like contractile phenotype. *Arterioscler. Thromb. Vasc. Biol.* **28**, 1505–1510 (2008). doi: [10.1161/ATVBAHA.108.166066](https://doi.org/10.1161/ATVBAHA.108.166066); pmid: [18451334](https://pubmed.ncbi.nlm.nih.gov/18451334/)
- L. S. Shankman et al., KLF4-dependent phenotypic modulation of smooth muscle cells has a key role in atherosclerotic plaque pathogenesis. *Nat. Med.* **21**, 628–637 (2015). doi: [10.1038/nm.3866](https://doi.org/10.1038/nm.3866); pmid: [25985364](https://pubmed.ncbi.nlm.nih.gov/25985364/)
- G. La Manno et al., RNA velocity of single cells. *Nature* **560**, 494–498 (2018). doi: [10.1038/s41586-018-0414-6](https://doi.org/10.1038/s41586-018-0414-6); pmid: [30089906](https://pubmed.ncbi.nlm.nih.gov/30089906/)
- S. Qunzain et al., CARMEN, a human super enhancer-associated long noncoding RNA controlling cardiac specification, differentiation and homeostasis. *J. Mol. Cell. Cardiol.* **89**, 98–112 (2015). doi: [10.1016/j.jmcc.2015.09.016](https://doi.org/10.1016/j.jmcc.2015.09.016); pmid: [26423156](https://pubmed.ncbi.nlm.nih.gov/26423156/)

45. M. T. Lawton *et al.*, Brain arteriovenous malformations. *Nat. Rev. Dis. Primers* **1**, 15008 (2015). doi: [10.1038/nrdp.2015.8](https://doi.org/10.1038/nrdp.2015.8); pmid: 27188382
46. J. E. Fish *et al.*, Somatic gain of KRAS function in the endothelium is sufficient to cause vascular malformations that require MEK but not PI3K signaling. *Circ. Res.* **127**, 727–743 (2020). doi: [10.1161/CIRCRESAHA.119.316500](https://doi.org/10.1161/CIRCRESAHA.119.316500); pmid: 32552404
47. P. A. Murphy *et al.*, Constitutively active Notch4 receptor elicits brain arteriovenous malformations through enlargement of capillary-like vessels. *Proc. Natl. Acad. Sci. U.S.A.* **111**, 18007–18012 (2014). doi: [10.1073/pnas.1415316111](https://doi.org/10.1073/pnas.1415316111); pmid: 25468970
48. H. Jiang *et al.*, MCH neurons regulate permeability of the median eminence barrier. *Neuron* **107**, 306–319.e9 (2020). doi: [10.1016/j.neuron.2020.04.020](https://doi.org/10.1016/j.neuron.2020.04.020); pmid: 32407670
49. E. I. Gaál *et al.*, Comparison of vascular growth factors in the murine brain reveals placenta growth factor as prime candidate for CNS revascularization. *Blood* **122**, 658–665 (2013). doi: [10.1182/blood-2012-07-441527](https://doi.org/10.1182/blood-2012-07-441527); pmid: 23803710
50. M. N. Jabbour *et al.*, Aberrant angiogenic characteristics of human brain arteriovenous malformation endothelial cells. *Neurosurgery* **64**, 139–148 (2009). doi: [10.1227/01.NEU.0000334417.56742.24](https://doi.org/10.1227/01.NEU.0000334417.56742.24); pmid: 19145162
51. L. D. Shoemaker, A. K. McCormick, B. M. Allen, S. D. Chang, Evidence for endothelial-to-mesenchymal transition in human brain arteriovenous malformations. *Clin. Transl. Med.* **10**, e99 (2020). doi: [10.1002/ctm2.99](https://doi.org/10.1002/ctm2.99); pmid: 32564509
52. R. Wright *et al.*, Histopathology of brain AVMs part II: Inflammation in arteriovenous malformation of the brain. *Acta Neurochir.* **162**, 1741–1747 (2020). doi: [10.1007/s00701-020-04328-3](https://doi.org/10.1007/s00701-020-04328-3); pmid: 32306161
53. S. Jin *et al.*, Inference and analysis of cell-cell communication using CellChat. *Nat. Commun.* **12**, 10088 (2021). doi: [10.1038/s41467-021-21246-9](https://doi.org/10.1038/s41467-021-21246-9); pmid: 33597522
54. A. M. Crist *et al.*, Angiopoietin-2 inhibition rescues arteriovenous malformation in a Smad4 hereditary hemorrhagic telangiectasia mouse model. *Circulation* **139**, 2049–2063 (2019). doi: [10.1161/CIRCULATIONAHA.118.036952](https://doi.org/10.1161/CIRCULATIONAHA.118.036952); pmid: 30744395
55. Y. Hwan Kim *et al.*, Overexpression of activin receptor-like kinase 1 in endothelial cells suppresses development of arteriovenous malformations in mouse models of hereditary hemorrhagic telangiectasia. *Circ. Res.* **127**, 1122–1137 (2020). doi: [10.1161/CIRCRESAHA.119.316267](https://doi.org/10.1161/CIRCRESAHA.119.316267); pmid: 32762495
56. W. Zhu *et al.*, Soluble FLT1 gene therapy alleviates brain arteriovenous malformation severity. *Stroke* **48**, 1420–1423 (2017). doi: [10.1161/STROKEAHA.116.015713](https://doi.org/10.1161/STROKEAHA.116.015713); pmid: 28325846
57. S. E. Marsh *et al.*, Single cell sequencing reveals glial specific responses to tissue processing and enzymatic dissociation in mice and humans. *bioRxiv* 408542 [Preprint] (2020). doi: [10.1101/2020.12.03.408542](https://doi.org/10.1101/2020.12.03.408542)
58. E. J. McMahon, S. L. Bailey, C. V. Castenada, H. Waldner, S. D. Miller, Epitope spreading initiates in the CNS in two mouse models of multiple sclerosis. *Nat. Med.* **11**, 335–339 (2005). doi: [10.1038/nm1202](https://doi.org/10.1038/nm1202); pmid: 15735651
59. C. Proding *et al.*, CD11c-expressing cells reside in the juxtavascular parenchyma and extend processes into the glia limitans of the mouse nervous system. *Acta Neuropathol.* **121**, 445–458 (2011). doi: [10.1007/s00401-010-0774-y](https://doi.org/10.1007/s00401-010-0774-y); pmid: 21076838
60. M. Majumdar, L. A. Tan, M. Chen, Critical assessment of the morbidity associated with ruptured cerebral arteriovenous malformations. *J. Neurointerv. Surg.* **8**, 163–167 (2016). doi: [10.1136/neurintsurg-2014-011517](https://doi.org/10.1136/neurintsurg-2014-011517); pmid: 25568227
61. D. J. Sokolowski *et al.*, Single-cell mapper (scMappR): Using scRNA-seq to infer the cell-type specificities of differentially expressed genes. *NAR Genom. Bioinform.* **3**, lqab011 (2021). doi: [10.1093/nargab/lqab011](https://doi.org/10.1093/nargab/lqab011); pmid: 33655208
62. R. N. Munji *et al.*, Profiling the mouse brain endothelial transcriptome in health and disease models reveals a core blood-brain barrier dysfunction module. *Nat. Neurosci.* **22**, 1892–1902 (2019). doi: [10.1038/s41593-019-0497-x](https://doi.org/10.1038/s41593-019-0497-x); pmid: 31611708
63. W. Chen *et al.*, Reduced mural cell coverage and impaired vessel integrity after angiogenic stimulation in the Akt1-deficient brain. *Arterioscler. Thromb. Vasc. Biol.* **33**, 305–310 (2013). doi: [10.1161/ATVBAHA.112.300485](https://doi.org/10.1161/ATVBAHA.112.300485); pmid: 23241407
64. J. Frösen, A. Joutel, Smooth muscle cells of intracranial vessels: From development to disease. *Cardiovasc. Res.* **114**, 501–512 (2018). doi: [10.1093/cvr/cvy002](https://doi.org/10.1093/cvr/cvy002); pmid: 29351598
65. Y. H. Zheng *et al.*, Osteopontin stimulates autophagy via integrin/CD44 and p38 MAPK signaling pathways in vascular smooth muscle cells. *J. Cell. Physiol.* **227**, 127–135 (2012). doi: [10.1002/jcp.22709](https://doi.org/10.1002/jcp.22709); pmid: 21374592
66. S. Bonney *et al.*, Diverse functions of retinoic acid in brain vascular development. *J. Neurosci.* **36**, 7786–7801 (2016). doi: [10.1523/JNEUROSCI.3952-15.2016](https://doi.org/10.1523/JNEUROSCI.3952-15.2016); pmid: 27445154
67. S. Mishra, Y. Choe, S. J. Pleasure, J. A. Siegenthaler, Cerebrovascular defects in Foxc1 mutants correlate with aberrant WNT and VEGF-A pathways downstream of retinoic acid from the meninges. *Dev. Biol.* **420**, 148–165 (2016). doi: [10.1016/j.ydbio.2016.09.019](https://doi.org/10.1016/j.ydbio.2016.09.019); pmid: 27671872
68. R. del Toro *et al.*, Identification and functional analysis of endothelial tip cell-enriched genes. *Blood* **116**, 4025–4033 (2010). doi: [10.1182/blood-2010-02-270819](https://doi.org/10.1182/blood-2010-02-270819); pmid: 20705756
69. M. Hupe *et al.*, Gene expression profiles of brain endothelial cells during embryonic development at bulk and single-cell levels. *Sci. Signal.* **10**, eaag2476 (2017). doi: [10.1126/scisignal.aag2476](https://doi.org/10.1126/scisignal.aag2476); pmid: 28698213
70. A. Bhaduri *et al.*, An atlas of cortical arealization identifies dynamic molecular signatures. *Nature* **598**, 200–204 (2021). doi: [10.1038/s41586-021-03910-8](https://doi.org/10.1038/s41586-021-03910-8); pmid: 34616070
71. J. J. Boyle, D. E. Bowyer, P. L. Weissberg, M. R. Bennett, Human blood-derived macrophages induce apoptosis in human plaque-derived vascular smooth muscle cells by Fas-ligand/Fas interactions. *Arterioscler. Thromb. Vasc. Biol.* **21**, 1402–1407 (2001). doi: [10.1161/hq0901.094279](https://doi.org/10.1161/hq0901.094279); pmid: 11557663
72. C. Soneson, A. Srivastava, R. Patro, M. B. Stadler, Preprocessing choices affect RNA velocity results for droplet scRNA-seq data. *PLOS Comput. Biol.* **17**, e1008585 (2021). doi: [10.1371/journal.pcbi.1008585](https://doi.org/10.1371/journal.pcbi.1008585); pmid: 33428615
73. A. Srivastava, L. Malik, T. Smith, I. Sudbery, R. Patro, Alevin efficiently estimates accurate gene abundances from dscRNA-seq data. *Genome Biol.* **20**, 65 (2019). doi: [10.1186/s13059-019-1670-y](https://doi.org/10.1186/s13059-019-1670-y); pmid: 30917859
74. N. J. Bernstein *et al.*, Solo: Doublet identification in single-cell RNA-seq via semi-supervised deep learning. *Cell Syst.* **11**, 95–101.e5 (2020). doi: [10.1016/j.cels.2020.05.010](https://doi.org/10.1016/j.cels.2020.05.010); pmid: 32592658
75. C. Hafemeister, R. Satija, Normalization and variance stabilization of single-cell RNA-seq data using regularized negative binomial regression. *Genome Biol.* **20**, 296 (2019). doi: [10.1186/s13059-019-1874-1](https://doi.org/10.1186/s13059-019-1874-1); pmid: 31870423
76. I. Korsunsky *et al.*, Fast, sensitive and accurate integration of single-cell data with Harmony. *Nat. Methods* **16**, 1289–1296 (2019). doi: [10.1038/s41592-019-0619-0](https://doi.org/10.1038/s41592-019-0619-0); pmid: 31740819
77. E. Becht *et al.*, Dimensionality reduction for visualizing single-cell data using UMAP. *Nat. Biotechnol.* **37**, 38–44 (2018). doi: [10.1038/nbt.4314](https://doi.org/10.1038/nbt.4314); pmid: 30531897
78. V. A. Traag, L. Waltman, N. J. van Eck, From Louvain to Leiden: Guaranteeing well-connected communities. *Sci. Rep.* **9**, 5233 (2019). doi: [10.1038/s41598-019-41695-z](https://doi.org/10.1038/s41598-019-41695-z); pmid: 30914743
79. V. Bergen, M. Lange, S. Peidli, F. A. Wolf, F. J. Theis, Generalizing RNA velocity to transient cell states through dynamical modeling. *Nat. Biotechnol.* **38**, 1408–1414 (2020). doi: [10.1038/s41587-020-0591-3](https://doi.org/10.1038/s41587-020-0591-3); pmid: 32747759
80. D. G. Bunis, J. Andrews, G. K. Fragiadakis, T. D. Burt, M. Sirota, dittoSeq: Universal user-friendly single-cell and bulk RNA sequencing visualization toolkit. *Bioinformatics* **36**, 5535–5536 (2020). doi: [10.1093/bioinformatics/btaa1011](https://doi.org/10.1093/bioinformatics/btaa1011); pmid: 33313640
81. G. Korotkevich *et al.*, Fast gene set enrichment analysis. *bioRxiv* 060012 [Preprint] (2021). doi: [10.1101/060012](https://doi.org/10.1101/060012)
82. M. Andreatta, S. J. Carmona, UCell: Robust and scalable single-cell gene signature scoring. *Comput. Struct. Biotechnol. J.* **19**, 3796–3798 (2021). doi: [10.1016/j.csbj.2021.06.043](https://doi.org/10.1016/j.csbj.2021.06.043); pmid: 34285779
83. R. Patro, G. Duggal, M. I. Love, R. A. Irizarry, C. Kingsford, Salmon provides fast and bias-aware quantification of transcript expression. *Nat. Methods* **14**, 417–419 (2017). doi: [10.1038/nmeth.4197](https://doi.org/10.1038/nmeth.4197); pmid: 28263959
84. C. Soneson, M. I. Love, M. D. Robinson, Differential analyses for RNA-seq: Transcript-level estimates improve gene-level inferences. *F1000Res.* **4**, 1521 (2015). doi: [10.12688/f1000research.7563.1](https://doi.org/10.12688/f1000research.7563.1); pmid: 26925227
85. M. D. Robinson, D. J. McCarthy, G. K. Smyth, edgeR: A Bioconductor package for differential expression analysis of digital gene expression data. *Bioinformatics* **26**, 139–140 (2010). doi: [10.1093/bioinformatics/btp166](https://doi.org/10.1093/bioinformatics/btp166); pmid: 19910308
86. C. Kim, Single cell atlas of the normal and malformed human brain vasculature, version 1, Zenodo (2022). doi: [10.5281/zenodo.5826205](https://doi.org/10.5281/zenodo.5826205)

ACKNOWLEDGMENTS

The authors acknowledge K. Probst and N. Srivastanti for creating schematics for the summary page figure and Figs. 1 and 3. **Funding:** This work was supported by National Institutes of Health grant U54NS065705 (E.A.W., H.K., and S.W.); National Institutes of Health grant ROINS034949 (H.K.); National Institutes of Health grant ROINS099268 (H.K.); National Institutes of Health grant RO1EB012031 (K.N.); National Institutes of Health grant ROINS034467 (B.V.Z.); National Institutes of Health grant 5PO1AG052350 (B.V.Z.); National Institutes of Health grant ROINS112357 (D.A.L.); National Institutes of Health grant F32CA228372 (E.A.W.); National Institutes of Health grant U01MH115747 (T.J.N.); Brain Aneurysm Foundation grant (E.A.W.); Veterans Affairs Merit award (D.A.L.); and gifts from the William K. Bowes Jr Foundation, the Shurl and Kay Curci Foundation, and Schmidt Futures (T.J.N.). **Author contributions:** Conceptualization: E.A.W., C.N.K., D.L.C., M.T.L., B.V.Z., A.A.A., D.A.L., and T.J.N. Methodology: E.A.W., C.N.K., I.O., L.Q.C., and T.J.N. Formal analysis: E.A.W., C.N.K., J.M.R., I.O., L.Q.C., and T.J.N. Investigation: E.A.W., C.N.K., J.M.R., J.H.G., E.G., I.O., L.Q.C., D.W., J.S.C., K.R., and K.N. Visualization: E.A.W., J.M.R., and C.N.K. Resources: A.A.A., E.F.C., M.T.L., and N.G. Funding acquisition: E.A.W., H.K., B.P.W., N.G., and T.J.N. Project administration: E.A.W., H.K., S.W., D.A.L., and T.J.N. Supervision: A.A.A., D.A.L., and T.J.N. Writing, original draft: E.A.W., C.N.K., T.N., and D.A.L. Writing, review and editing: E.A.W., C.N.K., J.S.C., K.R., K.N., H.K., D.L.C., M.T.L., N.G., B.V.Z., D.A.L., and T.J.N. **Competing interests:** The authors declare that they have no competing interests. **Data and materials availability:** Data are available to explore with an interactive cell viewer: <https://adult-brain-vasc.cells.ucsc.edu>. Sequencing data have been deposited at dbGAP phs002624.v2.p1. All code is available at <https://github.com/cnk113/vascular-analysis> and (86). All other data are available in the main text or the supplementary materials.

SUPPLEMENTARY MATERIALS

science.org/doi/10.1126/science.abi7377

Figs. S1 to S12

Tables S1 to S10

MDAR Reproducibility Checklist

[View/request a protocol for this paper from Bio-protocol.](#)

29 March 2021; resubmitted 23 September 2021

Accepted 19 January 2022

10.1126/science.abi7377

A single-cell atlas of the normal and malformed human brain vasculature

Ethan A. WinklerChang N. KimJayden M. RossJoseph H. GarciaEugene Gillrene OhLindsay Q. ChenDavid WuJoshua S. CatapanoKunal RaygorKazim NarsinhHelen KimShantel WeinsheimerDaniel L. CookeBrian P. WalcottMichael T. LawtonNalin GuptaBerislav V. ZlokovicEdward F. ChangAdib A. AblDaniel A. LimTomasz J. Nowakowski

Science, 375 (6584), eabi7377. • DOI: 10.1126/science.abi7377

Mapping the brain's blood vessels

Cerebrovascular diseases are a leading cause of death and disability, but our understanding of the cellular and molecular constituents of normal and diseased human cerebrovasculature is incomplete. Winkler *et al.* generated a cellular-resolution atlas of the adult human cerebrovasculature. The authors used spatial transcriptomics to reveal the geographical organization of an unexpectedly diverse array of molecularly defined cell types within the human brain. They then explored the cellular and molecular alterations that occur in arteriovenous malformations, a leading cause of stroke in young people. A specialized subtype of peripheral monocyte plays a role in destabilizing the cerebrovasculature, and the authors identified candidate targets for therapeutic intervention. —STS

View the article online

<https://www.science.org/doi/10.1126/science.abi7377>

Permissions

<https://www.science.org/help/reprints-and-permissions>

Use of this article is subject to the [Terms of service](#)

Science (ISSN) is published by the American Association for the Advancement of Science. 1200 New York Avenue NW, Washington, DC 20005. The title *Science* is a registered trademark of AAAS.

Copyright © 2022 The Authors, some rights reserved; exclusive licensee American Association for the Advancement of Science. No claim to original U.S. Government Works